SANDIA REPORT
SAND2024-xxxx
Printed September 2024

Sandia National Laboratories

Level 2 Milestone: Develop and Incorporate Novel Code Verification of Fundamental Equations in Gemma and Set Up Appropriate Tests

Brian A. Freno, Neil R. Matula, Aaron M. Krueger

Prepared by
Sandia National Laboratories
Albuquerque, New Mexico 87185
Livermore, California 94550

Issued by Sandia National Laboratories, operated for the United States Department of Energy by National Technology & Engineering Solutions of Sandia, LLC.

Available to DOE and DOE contractors from

U.S. Department of Energy
Office of Scientific and Technical Information
P.O. Box 62
Oak Ridge, TN 37831

Telephone: (865) 576-8401
Facsimile: (865) 576-5728
E-Mail: reports@osti.gov
Online ordering: http://www.osti.gov/scitech

Available to the public from

U.S. Department of Commerce
National Technical Information Service
5301 Shawnee Road
Alexandria, VA 22312

Telephone: (800) 553-6847
Facsimile: (703) 605-6900
E-Mail: orders@ntis.gov
Online order: https://classic.ntis.gov/help/order-methods

ABSTRACT

For computational physics simulations, code verification plays a major role in establishing the credibility of the results by assessing the correctness of the implementation of the underlying numerical methods. In computational electromagnetics, surface integral equations, such as the method-of-moments implementations of the electric-, magnetic-, and combined-field integral equations, are frequently used to solve Maxwell's equations on the surfaces of electromagnetic scatterers. These electromagnetic surface integral equations yield many code-verification challenges due to the various sources of numerical error and their possible interactions. In this report, we provide approaches to separately measure the numerical errors arising from these different error sources. We demonstrate the effectiveness of these approaches in Gemma.

ACKNOWLEDGMENTS

The authors would like to thank the members of the milestone review team, Bill Rider, Jim Ferguson, Shawn Pautz, and Duncan McGregor, as well as members of the Plasma / Electromagnetics Software department, Rob Pfeiffer, Joe Kotulski, and Evelyn Dohme, for taking the time to thoughtfully assess our work and to provide valuable feedback.

CONTENTS

LIST OF FIGURES

1. INTRODUCTION

1.1. Gemma

Gemma is a computational electromagnetics code that simulates three-dimensional scattering problems by solving electromagnetic surface integral equations in the frequency domain. It is designed to be massively parallel and to run on heterogeneous computer architectures. Gemma is part of the Radiation Analysis Modeling and Simulation of Electrical Systems (RAMSES) tool suite, which is used to support the nuclear-deterrence mission at Sandia National Laboratories. In this report, we present our code-verification activities for Gemma.

1.2. Electromagnetic Surface Integral Equations

For electromagnetic scatterers, Maxwell's equations, together with appropriate boundary conditions, may be formulated as surface integral equations (SIEs). The most common SIEs for modeling time-harmonic electromagnetic phenomena are the electric-field integral equation (EFIE), which relates the surface current to the scattered electric field, and the magnetic-field integral equation (MFIE), which relates the surface current to the scattered magnetic field. The EFIE arises from the condition that the total tangential electric field on the surface of a perfect electric conductor is zero, whereas the MFIE arises from the condition that the component of the total magnetic field tangent to the surface of a perfect electric conductor is equal to the surface current density. At certain frequencies, the accuracy of the solutions to the EFIE and MFIE deteriorates due to the internal resonances of the scatterer. Therefore, the combined-field integral equation (CFIE), which is a linear combination of the EFIE and MFIE, is employed to overcome this problem.

These SIEs are typically solved through the method of moments (MoM), wherein the surface of the electromagnetic scatterer is discretized using planar or curvilinear mesh elements, and four-dimensional integrals are evaluated over two-dimensional source and test elements. These integrals contain a Green's function, which yields singularities when the test and source elements share one or more edges or vertices, and near-singularities when they are otherwise close. The accurate evaluation of these integrals is an active research topic, with many approaches being developed to address the (near-)singularity for the inner, source-element integral [1–10], as well as for the outer, test-element integral [11–15].

1.3. Code Verification

For computational physics codes in general, it is necessary to assess the implementation and the suitability of the underlying models in order to develop confidence in the simulation results. These assessments typically fall into two complementary categories: verification and validation. Validation evaluates the appropriateness of the models instantiated in the code for representing the relevant physical phenomena, and is typically performed through comparison with experimental data. Verification, on the other hand, assesses the correctness of the numerical solutions produced by the code, through comparison with the expected theoretical behavior of the implemented numerical methods. Following Roache [16], Knupp and Salari [17], and Oberkampf and Roy [18], verification can be further divided into the activities of code verification and solution verification. Solution verification involves the estimation of the numerical error for a particular simulation, whereas code verification assesses the correctness of the implementation of the numerical methods within the code. Code verification ultimately sets the expectations for solution verification. A review of code and solution verification is presented by Roy [19].

Code verification is the primary focus of this report. Differential, integral, and integro-differential equations may be solved exactly only in special cases. In the general case, the integral and differential operators must be approximated by discrete operators to yield a tractable system of equations. The difference between the discrete and continuous operators is the truncation error. As a result of the truncation error, even if the discretized equations are solved exactly, the resulting solution will only approximately satisfy the original continuous equations, introducing a discretization error – the difference between the solution to the discrete equations and the solution to the continuous equations. If the discretization error tends to zero as the discretization is refined, the consistency of the code is verified [16]. This may be taken a step further by examining not only consistency, but the rate at which the error decreases as the discretization is refined, thereby verifying the order of accuracy of the discretization scheme. The correctness of the numerical-method implementation may then be verified by comparing the expected and observed orders of accuracy obtained from numerous test cases with known solutions.

In addition to assessing the suitability and correctness of the numerical methods, the error measured from code-verification activities enables the accuracy of different algorithms to be compared and provides an initial error estimate for solution-verification activities.

1.4. Manufactured Solutions

Exact solutions to systems of engineering interest are rare, and those that do exist often require dramatic simplifications to both the domain geometry and the equations themselves in order to obtain a tractable problem. Hence, manufactured solutions are frequently employed to produce problems of sufficient complexity with known solutions [20]. The method of manufactured solutions (MMS) is a general technique for constructing problems of arbitrary complexity with known solutions. One begins this process in reverse by manufacturing

the desired solution. In principle, this manufactured solution (MS) may be any function, but several properties are desirable [17]:

1. The MS should consist of combinations of elementary functions, such as polynomial, trigonometric, and exponential functions. This not only simplifies derivations and implementation, but ensures that the MS (and its derivatives) will be representable to sufficient precision within the tested code.

2. The MS should be sufficiently smooth, such that the error incurred by the discretization is small on relatively coarse meshes. This ensures that the order of accuracy may be estimated with minimal computational expense.

3. The MS should be general enough that all terms of the governing equations are exercised.

4. The MS should have a sufficient number of nontrivial derivatives, such that the expected order of accuracy of the discretization can be observed. In the most ideal case, the solution will have an infinite number of nontrivial derivatives.

5. Since the robustness of the code is not the primary concern, the MS should not have any features that inhibit the solution of the discretized equations.

Once a solution is manufactured, it is substituted directly into the governing equations. In general, the MS is not expected to satisfy the governing equations. Instead, a residual term appears, which quantifies the deviation from the satisfaction of the equations. If this residual is added to the governing equations as a source term, the resulting equations will be exactly satisfied by the MS. Concerns are immediately raised regarding uniqueness of the solution to the manufactured problem, but this has rarely been found to cause difficulties in practice [20]. The result of this process is a problem, of arbitrary complexity, for which an exact solution is known.

The code to be verified is then modified to support the additional source term and may then be verified by comparing the simulation result for the manufactured problem against the known solution. Ideally, the source term is computed analytically; however, when this is not possible, the source term needs to be computed consistently and at least as accurately as the numerical methods being verified. Otherwise, the error in the source term will overshadow that of the numerical methods, contaminating the verification assessment.

MMS is purely a mathematical process; the physics of the problem need not be considered, provided the MS remains within the bounds of validity for the underlying algorithms. This enables the user to avoid difficulties that would normally complicate the solution.

1.5. Code Verification for Electromagnetic Integral Equations

There are many examples of code verification in the literature for different computational physics disciplines. These disciplines include aerodynamics [21], fluid dynamics [22–28],

solid mechanics [29], fluid–structure interaction [30, 31], heat transfer in fluid–solid interaction [32], multiphase flows [33, 34], radiation hydrodynamics [35], plasma physics [36–39], electrodynamics [40], and ablation [41–45].

However, existing literature contains few instances of MMS being used in the verification of software for integral equations. This is due to the simple fact that, while analytical differentiation is a straightforward exercise, analytical integration is not always possible. Hence, the residual source term arising from the manufactured solution may not be representable in closed form, and its implementation may be accompanied by numerical techniques that carry their own uncertainties. Furthermore, for the EFIE, MFIE, and CFIE, the aforementioned (nearly) singular integrals can further complicate the numerical evaluation of the source term. Therefore, much of the elegance, simplicity, and instilled confidence of MMS is lost when applied to integral equations in a straightforward manner, and, as a result, effective implementation of MMS in the context of boundary element codes has been an open subject of research.

Prior to our work, the most substantial code-verification effort for integral equations in computational electromagnetics was the work of Marchand et al. [46, 47], in which the authors calculate the MMS source terms for the EFIE using numerical techniques. While the quadrature error can be driven low enough that mesh-refinement studies become feasible, the presence of this additional error often places a lower bound on the discretization error that can be obtained, and therefore limits the scope of the mesh-refinement study, in addition to being undesirable for the aforementioned reasons. To further complicate matters, for the MoM implementation of the EFIE, the discretized equations can easily become ill-conditioned [48].

For the MoM implementation of the electromagnetic integral equations, numerical error is introduced from three sources:

1. **Domain discretization.** While planar surfaces can be represented exactly by planar elements, the approximation of sufficiently smooth curved surfaces with planar elements introduces a second-order numerical error [49, Chap. 3]. This error can be reduced by employing curved elements [50].

2. **Solution discretization.** Common in the solution to differential, integral, and integro-differential equations, the approximation of the solution in terms of a finite number of basis functions, or alternatively the approximation of the underlying equation operators in terms of a finite amount of solution queries, is the most common contributor to the numerical error. For sufficiently smooth solutions, this error can be reduced by employing higher-order basis functions [50] or stencils.

3. **Numerical integration.** The analytical evaluation of the integrals in integral equations is usually not possible. For well-behaved integrals, quadrature rules or other integration methods can be used, with the expectation that the associated numerical error is at least of the same order as that arising from the solution-discretization error. A less rigorous expectation is that the error from numerical integration decreases as the fidelity of

the numerical integration algorithm is increased (e.g., increasing the number of quadrature points). However, for singular or nearly singular integrals, such convergence is not assured [51].

It is important to account for these error sources when performing code verification.

For the EFIE, Freno et al. [52] manufacture the Green's function, permitting the numerical-integration error to be eliminated and the solution-discretization error to be isolated. Freno et al. [53] also provide approaches to isolate the numerical-integration error. For the MFIE and CFIE, Freno and Matula [54, 55] isolate and measure the solution-discretization error and numerical-integration error.

1.6. This Work

In this report, we present code-verification techniques for the method-of-moments implementation of the EFIE, MFIE, and CFIE that isolate and measure the solution-discretization error and numerical-integration error. We manufacture the electric surface current density, which yields a source term that we can treat as a manufactured incident field. For curved surfaces, the domain-discretization error cannot be completely isolated or eliminated, but methods are presented in [54] to account for it in the MFIE. These methods can be applied to the other SIEs straightforwardly. In this report, we avoid the domain-discretization error by considering only planar surfaces. As in [52, 54, 56], we isolate the solution-discretization error by manufacturing the Green's function in terms of even powers of the distance between the test and source points. With this form, we can evaluate the integrals exactly, thereby avoiding numerical-integration error. We isolate the numerical-integration error on both sides of the equations by canceling the influence of the basis functions. This approach has been demonstrated for the MFIE [54], CFIE [55], and EFIE [56]. With the solution-discretization error and numerical-integration error isolated, we perform convergence studies for different manufactured Green's functions and geometries.

This report is organized as follows. In Chapter 2, we describe the EFIE, MFIE, and CFIE and their discretization. In Chapter 3, we describe the challenges of using MMS with these equations, as well as our approaches to mitigating them. In Chapter 4, we demonstrate the effectiveness of our approaches in Gemma for several different configurations. In Chapter 5, we summarize this work.

2. THE METHOD-OF-MOMENTS IMPLEMENTATION OF THE ELECTRIC-, MAGNETIC-, AND COMBINED-FIELD INTEGRAL EQUATIONS

In time-harmonic form, the scattered electric field $\mathbf{E}^{\mathcal{S}}$ and magnetic field $\mathbf{H}^{\mathcal{S}}$ due to induced surface currents on a scatterer can be computed by [57]

$$\mathbf{E}^{\mathcal{S}}(\mathbf{x}) = -(j\omega\mathbf{A}(\mathbf{x}) + \nabla\Phi(\mathbf{x})), \tag{2.1}$$

$$\mathbf{H}^{\mathcal{S}}(\mathbf{x}) = \frac{1}{\mu}\nabla \times \mathbf{A}(\mathbf{x}), \tag{2.2}$$

where the magnetic vector potential $\mathbf{A}$ is defined by

$$\mathbf{A}(\mathbf{x}) = \mu \int_{S'} \mathbf{J}(\mathbf{x}')G(\mathbf{x}, \mathbf{x}')dS', \tag{2.3}$$

and, by employing the Lorenz gauge condition and the continuity equation, the electric scalar potential Φ is defined by

$$\Phi(\mathbf{x}) = \frac{j}{\epsilon\omega} \int_{S'} \nabla' \cdot \mathbf{J}(\mathbf{x}')G(\mathbf{x}, \mathbf{x}')dS'. \tag{2.4}$$

In (2.3) and (2.4), the integration domain $S' = S$ is the closed surface of a perfect electric conductor, where the prime notation is introduced here to distinguish the inner and outer integration domains later in this section. Additionally, $\mathbf{J}$ is the electric surface current density, μ and ϵ are the permeability and permittivity of the surrounding medium, and G is the Green's function

$$G(\mathbf{x}, \mathbf{x}') = \frac{e^{-jkR}}{4\pi R}, \tag{2.5}$$

where $R = \|\mathbf{R}\|_2$, $\mathbf{R} = \mathbf{x} - \mathbf{x}'$, and $k = \omega\sqrt{\mu\epsilon}$ is the wavenumber.

2.1. The Electric-Field Integral Equation

The total electric field $\mathbf{E}$ is the sum of the incident electric field $\mathbf{E}^{\mathcal{I}}$, which induces $\mathbf{J}$, and $\mathbf{E}^{\mathcal{S}}$. On S, the tangential component of $\mathbf{E}$ is zero, such that

$$\mathbf{E}_t^{\mathcal{S}} = -\mathbf{E}_t^{\mathcal{I}}, \tag{2.6}$$

where $(\cdot)_t$ denotes the tangential component. Substituting (2.1) into (2.6) yields the EFIE at a point on the surface of the scatterer, from which we can compute $\mathbf{J}$ from $\mathbf{E}^{\mathcal{I}}$:

$$(j\omega\mathbf{A} + \nabla\Phi)_t = \mathbf{E}_t^{\mathcal{I}}. \tag{2.7}$$

2.2. The Magnetic-Field Integral Equation

The total magnetic field $\mathbf{H}$ is the sum of the incident magnetic field $\mathbf{H}^{\mathcal{I}}$ and $\mathbf{H}^{\mathcal{S}}$. On S,

$$\mathbf{n} \times \mathbf{H} = \mathbf{J}, \tag{2.8}$$

where $\mathbf{n}$ is the unit vector normal to S. Noting that $\nabla \times \Big[\mathbf{J}(\mathbf{x}')G(\mathbf{x},\mathbf{x}')\Big] = \nabla G(\mathbf{x},\mathbf{x}') \times \mathbf{J}(\mathbf{x}')$ and

$$\nabla G(\mathbf{x},\mathbf{x}') = -\nabla' G(\mathbf{x},\mathbf{x}'), \tag{2.9}$$

from (2.2) and (2.3),

$$\mathbf{H}^{\mathcal{S}}(\mathbf{x}) = \int_{S'} \mathbf{J}(\mathbf{x}') \times \nabla' G(\mathbf{x},\mathbf{x}') dS'$$

when $\mathbf{x}$ is just outside of S. Therefore, at S,

$$\mathbf{n} \times \mathbf{H}^{\mathcal{S}} = \lim_{\mathbf{x}\to S} \mathbf{n} \times \int_{S'} \mathbf{J}(\mathbf{x}') \times \nabla' G(\mathbf{x},\mathbf{x}') dS' = \frac{1}{2}\mathbf{J} + \mathbf{n} \times \int_{S'} \mathbf{J}(\mathbf{x}') \times \nabla' G(\mathbf{x},\mathbf{x}') dS', \tag{2.10}$$

where the final term is evaluated through principal value integration. From (2.8) and (2.10) the MFIE at a point on the surface of the scatterer is [58, 59]

$$\frac{1}{2}\mathbf{J} - \mathbf{n} \times \int_{S'} \mathbf{J}(\mathbf{x}') \times \nabla' G(\mathbf{x},\mathbf{x}') dS' = \mathbf{n} \times \mathbf{H}^{\mathcal{I}}. \tag{2.11}$$

2.3. The Method of Moments

Inserting (2.3) and (2.4) into (2.7), projecting (2.7) onto an appropriate space $\mathbb{V}$ containing vector fields that are tangent to S, and integrating by parts yields the variational form of the EFIE: find $\mathbf{J} \in \mathbb{V}$, such that

$$\int_S \mathbf{E}^{\mathcal{I}} \cdot \bar{\mathbf{v}} dS =$$

$$j\omega\mu \int_S \bar{\mathbf{v}}(\mathbf{x}) \cdot \int_{S'} \mathbf{J}(\mathbf{x}') G(\mathbf{x},\mathbf{x}') dS' dS - \frac{j}{\epsilon\omega} \int_S \nabla \cdot \bar{\mathbf{v}}(\mathbf{x}) \int_{S'} \nabla' \cdot \mathbf{J}(\mathbf{x}') G(\mathbf{x},\mathbf{x}') dS' dS \tag{2.12}$$

for all $\mathbf{v} \in \mathbb{V}$, where the overbar denotes complex conjugation.

We can write (2.12) more succinctly in terms of a sesquilinear form and inner product:

$$a^{\mathcal{E}}(\mathbf{J},\mathbf{v}) = b^{\mathcal{E}}\Big(\mathbf{E}^{\mathcal{I}},\mathbf{v}\Big), \tag{2.13}$$

where the sesquilinear form and inner product are defined by

$$\begin{aligned}
a^{\mathcal{E}}(\mathbf{u},\mathbf{v}) &= a^{\mathbf{A}}(\mathbf{u},\mathbf{v}) + a^{\Phi}(\mathbf{u},\mathbf{v}), \\
a^{\mathbf{A}}(\mathbf{u},\mathbf{v}) &= j\omega\mu \int_S \bar{\mathbf{v}}(\mathbf{x}) \cdot \int_{S'} \mathbf{u}(\mathbf{x}') G(\mathbf{x},\mathbf{x}') dS' dS, \\
a^{\Phi}(\mathbf{u},\mathbf{v}) &= -\frac{j}{\epsilon\omega} \int_S \nabla \cdot \bar{\mathbf{v}}(\mathbf{x}) \int_{S'} \nabla' \cdot \mathbf{u}(\mathbf{x}') G(\mathbf{x},\mathbf{x}') dS' dS, \\
b^{\mathcal{E}}(\mathbf{u},\mathbf{v}) &= \int_S \mathbf{u}(\mathbf{x}) \cdot \bar{\mathbf{v}}(\mathbf{x}) dS.
\end{aligned} \tag{2.14}$$

Projecting (2.11) onto $\mathbb{V}$ yields the variational form of the MFIE: find $\mathbf{J} \in \mathbb{V}$, such that

$$\frac{1}{2}\int_S \bar{\mathbf{v}} \cdot \mathbf{J} dS - \int_S \bar{\mathbf{v}}(\mathbf{x}) \cdot \left(\mathbf{n}(\mathbf{x}) \times \int_{S'} \mathbf{J}(\mathbf{x}') \times \nabla' G(\mathbf{x}, \mathbf{x}') dS'\right) dS = \int_S \bar{\mathbf{v}} \cdot \Big(\mathbf{n} \times \mathbf{H}^{\mathcal{I}}\Big) dS \quad (2.15)$$

for all $\mathbf{v} \in \mathbb{V}$. We can write (2.15) more succinctly as

$$a^{\mathcal{M}}(\mathbf{J}, \mathbf{v}) = b^{\mathcal{M}}\Big(\mathbf{H}^{\mathcal{I}}, \mathbf{v}\Big), \quad (2.16)$$

where the sesquilinear forms are defined by

$$a^{\mathcal{M}}(\mathbf{u}, \mathbf{v}) = \frac{1}{2}\int_S \bar{\mathbf{v}}(\mathbf{x}) \cdot \mathbf{u}(\mathbf{x}) dS - \int_S \bar{\mathbf{v}}(\mathbf{x}) \cdot \left(\mathbf{n}(\mathbf{x}) \times \int_{S'} \mathbf{u}(\mathbf{x}') \times \nabla' G(\mathbf{x}, \mathbf{x}') dS'\right) dS, \quad (2.17)$$

$$b^{\mathcal{M}}(\mathbf{u}, \mathbf{v}) = \int_S \bar{\mathbf{v}}(\mathbf{x}) \cdot [\mathbf{n}(\mathbf{x}) \times \mathbf{u}(\mathbf{x})] dS.$$

2.4. The Combined-Field Integral Equation

The CFIE linearly combines the EFIE (2.13) and MFIE (2.16) to yield the variational problem: find $\mathbf{J} \in \mathbb{V}$, such that

$$a(\mathbf{J}, \mathbf{v}) = b\Big(\mathbf{E}^{\mathcal{I}}, \mathbf{H}^{\mathcal{I}}, \mathbf{v}\Big) \qquad \forall \mathbf{v} \in \mathbb{V}, \quad (2.18)$$

where

$$a(\mathbf{J}, \mathbf{v}) = \frac{\alpha}{\eta} a^{\mathcal{E}}(\mathbf{J}, \mathbf{v}) + (1 - \alpha) a^{\mathcal{M}}(\mathbf{J}, \mathbf{v}), \quad (2.19)$$

$$b\Big(\mathbf{E}^{\mathcal{I}}, \mathbf{H}^{\mathcal{I}}, \mathbf{v}\Big) = \frac{\alpha}{\eta} b^{\mathcal{E}}\Big(\mathbf{E}^{\mathcal{I}}, \mathbf{v}\Big) + (1 - \alpha) b^{\mathcal{M}}\Big(\mathbf{H}^{\mathcal{I}}, \mathbf{v}\Big). \quad (2.20)$$

In (2.19) and (2.20), $\alpha \in [0, 1]$ is the combination parameter, and $\eta = \sqrt{\mu/\epsilon}$ is the characteristic impedance of the surrounding medium. It should be noted this is one of multiple choices for the CFIE [60, 61]; however, the verification methods presented in this report can be applied to the other CFIE choices.

In (2.18), setting $\alpha = 0$ yields the variational form of the MFIE. To simplify the notation in this report, we use (2.18) to represent the CFIE, MFIE, and EFIE. For the EFIE, we set $\alpha = 1$ and implicitly multiply (2.18) by η to remove the $1/\eta$ factor.

2.5. Discretization

To solve the variational problem (2.18), we discretize S with a mesh composed of triangular elements and approximate $\mathbf{J}$ with $\mathbf{J}_h$ in terms of the Rao–Wilton–Glisson (RWG) basis functions $\mathbf{\Lambda}_j(\mathbf{x})$ [3]:

$$\mathbf{J}_h(\mathbf{x}) = \sum_{j=1}^{n_b} J_j \mathbf{\Lambda}_j(\mathbf{x}), \quad (2.21)$$

where n_b is the total number of basis functions. The RWG basis functions are second-order accurate [49, pp. 155–156], and are defined for a triangle pair by

$$\mathbf{\Lambda}_j(\mathbf{x}) = \begin{cases} \dfrac{\ell_j}{2A_j^+}\boldsymbol{\rho}_j^+, & \text{for } \mathbf{x} \in T_j^+ \\ \dfrac{\ell_j}{2A_j^-}\boldsymbol{\rho}_j^-, & \text{for } \mathbf{x} \in T_j^- \\ \mathbf{0}, & \text{otherwise} \end{cases},$$

where ℓ_j is the length of the edge shared by the triangle pair, and A_j^+ and A_j^- are the areas of the triangles T_j^+ and T_j^- associated with basis function j. $\boldsymbol{\rho}_j^+$ denotes the vector from the vertex of T_j^+ opposite the shared edge to $\mathbf{x}$, and $\boldsymbol{\rho}_j^-$ denotes the vector to the vertex of T_j^- opposite the shared edge from $\mathbf{x}$.

These basis functions ensure that $\mathbf{J}_h$ is tangent to the mesh when using planar triangular elements. Additionally, along the shared edge of the triangle pair, the component of $\mathbf{\Lambda}_j(\mathbf{x})$ normal to that edge is unity. Therefore, for a triangle edge shared by only two triangles, the component of $\mathbf{J}_h$ normal to that edge is J_j. The solution is considered most accurate at the midpoint of the edge [49, pp. 155–156]; therefore, we measure the solution at the midpoints.

Defining $\mathbb{V}_h$ to be the span of RWG basis functions associated with the mesh on S, the Galerkin approximation of (2.18) is now: find $\mathbf{J}_h \in \mathbb{V}_h$, such that

$$a(\mathbf{J}_h, \mathbf{\Lambda}_i) = b\Big(\mathbf{E}^{\mathcal{I}}, \mathbf{H}^{\mathcal{I}}, \mathbf{\Lambda}_i\Big) \tag{2.22}$$

for $i = 1, \ldots, n_b$. Letting $\mathbf{J}^h$ denote the vector of coefficients used to construct $\mathbf{J}_h$ (2.21), (2.22) can be written in matrix form as $\mathbf{Z}\mathbf{J}^h = \mathbf{V}$, where $Z_{i,j} = a(\mathbf{\Lambda}_j, \mathbf{\Lambda}_i)$ is the impedance matrix, $J_j^h = J_j$ is the current vector, and $V_i = b\Big(\mathbf{E}^{\mathcal{I}}, \mathbf{H}^{\mathcal{I}}, \mathbf{\Lambda}_i\Big)$ is the excitation vector.

3. MANUFACTURED SOLUTIONS

We define the residual functional for each test basis function as

$$r_i(\mathbf{u}) = a(\mathbf{u}, \mathbf{\Lambda}_i) - b\Big(\mathbf{E}^{\mathcal{I}}, \mathbf{H}^{\mathcal{I}}, \mathbf{\Lambda}_i\Big). \tag{3.1}$$

We can write the variational form (2.18) in terms of (3.1) as

$$r_i(\mathbf{J}) = a(\mathbf{J}, \mathbf{\Lambda}_i) - b\Big(\mathbf{E}^{\mathcal{I}}, \mathbf{H}^{\mathcal{I}}, \mathbf{\Lambda}_i\Big) = 0. \tag{3.2}$$

Similarly, we can write the discretized problem (2.22) in terms of (3.1) as

$$r_i(\mathbf{J}_h) = a(\mathbf{J}_h, \mathbf{\Lambda}_i) - b\Big(\mathbf{E}^{\mathcal{I}}, \mathbf{H}^{\mathcal{I}}, \mathbf{\Lambda}_i\Big) = 0. \tag{3.3}$$

The method of manufactured solutions modifies (3.3) to be

$$r_i(\mathbf{J}_h) = r_i(\mathbf{J}_{\text{MS}}), \tag{3.4}$$

where $\mathbf{J}_{\text{MS}}$ is the manufactured solution, and $\mathbf{r}(\mathbf{J}_{\text{MS}})$ is computed exactly.

Inserting (3.2) and (3.3) into (3.4) yields

$$a(\mathbf{J}_h, \mathbf{\Lambda}_i) = a(\mathbf{J}_{\text{MS}}, \mathbf{\Lambda}_i). \tag{3.5}$$

However, instead of solving (3.5), we can equivalently solve (2.22) by setting

$$b\Big(\mathbf{E}^{\mathcal{I}}, \mathbf{H}^{\mathcal{I}}, \mathbf{\Lambda}_i\Big) = a(\mathbf{J}_{\text{MS}}, \mathbf{\Lambda}_i). \tag{3.6}$$

Equation (3.6) is satisfied by [52]

$$\mathbf{E}^{\mathcal{I}} = \frac{j}{\epsilon\omega} \int_{S'} \Big[k^2 \mathbf{J}_{\text{MS}}(\mathbf{x}') G(\mathbf{x}, \mathbf{x}') + \nabla' \cdot \mathbf{J}_{\text{MS}}(\mathbf{x}') \nabla G(\mathbf{x}, \mathbf{x}')\Big] dS',$$

which, from (2.9), is equivalent to

$$\mathbf{E}^{\mathcal{I}} = \frac{j}{\epsilon\omega} \int_{S'} \Big[k^2 \mathbf{J}_{\text{MS}}(\mathbf{x}') G(\mathbf{x}, \mathbf{x}') - \nabla' \cdot \mathbf{J}_{\text{MS}}(\mathbf{x}') \nabla' G(\mathbf{x}, \mathbf{x}')\Big] dS', \tag{3.7}$$

and [54]

$$\mathbf{H}^{\mathcal{I}} = \frac{1}{2} \mathbf{J}_{\text{MS}} \times \mathbf{n} - \int_{S'} \mathbf{J}_{\text{MS}}(\mathbf{x}') \times \nabla' G(\mathbf{x}, \mathbf{x}') dS'. \tag{3.8}$$

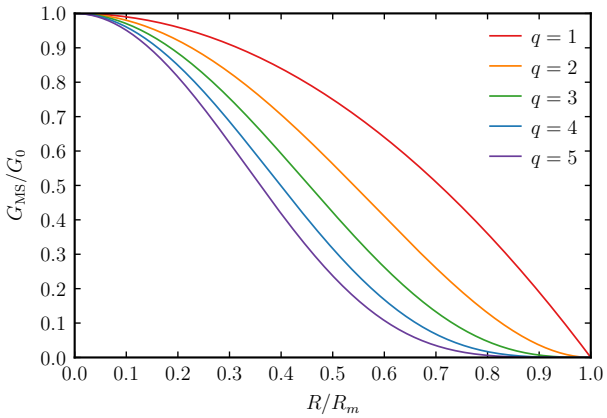

Figure 3-1. G_{MS} (3.9) for different values of q.

3.1. Manufactured Green's Function

Integrals containing the Green's function (2.5) or its derivatives, such as those appearing in $a(\cdot,\cdot)$ (2.19) and $b(\cdot,\cdot,\cdot)$ (2.20) cannot be computed analytically. Additionally, the singularity when $R \to 0$ complicates their accurate approximation, potentially contaminating convergence studies. Therefore, as is done in [52, 54, 56], we manufacture the Green's function, using the form

$$G_{\mathrm{MS}}(\mathbf{x},\mathbf{x}') = G_q(\mathbf{x},\mathbf{x}') = G_0\left(1 - \frac{R^2}{R_m^2}\right)^q, \tag{3.9}$$

where $G_0 = 1\ \mathrm{m}^{-1}$, $q \in \mathbb{N}$, and $R_m = \max_{\mathbf{x},\mathbf{x}' \in S} R$ is the maximum possible distance between two points on the domain. The even powers of R permit the aforementioned integrals to be computed analytically for the basis functions, as well as for many choices of $\mathbf{J}_{\mathrm{MS}}$, avoiding contamination from numerical-integration error. A plot of (3.9) is shown in Figure 3-1 for multiple values of q.

3.2. Solution-Discretization Error

In (2.22), if the integrals in $a(\cdot,\cdot)$ (2.19) and $b(\cdot,\cdot,\cdot)$ (2.20) are evaluated exactly, the only contribution to the discretization error is the solution-discretization error. Solving for $\mathbf{J}^h$ enables us to compute the discretization error

$$\mathbf{e}_{\mathbf{J}} = \mathbf{J}^h - \mathbf{J}_n, \tag{3.10}$$

where J_{n_j} denotes the component of $\mathbf{J}_{\mathrm{MS}}$ flowing from T_j^+ to T_j^-. The norm of (3.10) has the property $\|\mathbf{e}_{\mathbf{J}}\| \leq C_{\mathbf{J}} h^{p_{\mathbf{J}}}$, where $C_{\mathbf{J}}$ is a function of the solution derivatives, h is representative of the mesh size, and $p_{\mathbf{J}}$ is the order of accuracy. By performing a mesh-convergence study of the norm of the discretization error, we can ensure the expected order of accuracy is obtained. For the RWG basis functions, the expectation is second-order accuracy ($p_{\mathbf{J}} = 2$) when the error is evaluated at the edge centers [49].

3.3. Solution Uniqueness

For the EFIE, the manufactured Green's function G_{MS} (3.9) yields a matrix that is practically singular, admitting infinite solutions $\mathbf{J}^h$. For the MFIE, the matrix arising from only the first term of (2.17), which does not contain a Green's function, is nonsingular. Additionally, the matrix arising from the first and second terms is nonsingular when G_{MS} is used. However, the matrix arising from only the second term is practically singular.

In [52, 62], a mitigation approach is presented to select $\mathbf{J}^h$, by solving the optimization problem

$$\begin{aligned} &\text{minimize} && \|\mathbf{e}_{\mathbf{J}}\|_2 \\ &\text{subject to} && a(\mathbf{J}_h, \mathbf{\Lambda}_i) = b\Big(\mathbf{E}^{\mathcal{I}}, \mathbf{H}^{\mathcal{I}}, \mathbf{\Lambda}_i\Big). \end{aligned} \tag{3.11}$$

The solution to (3.11) is

$$\mathbf{J}^h = \mathbf{J}_n + \mathbf{Q}_1\Big(\mathbf{u} - \mathbf{Q}_1^H \mathbf{J}_n\Big),$$

where $\mathbf{R}_1^H \mathbf{u} = \mathbf{P}^T \mathbf{V}$ and $\mathbf{Q}_1$, $\mathbf{R}_1$, and $\mathbf{P}$ arise from the pivoted QR factorization of $\mathbf{Z}^H$.

In formulating the optimization problem (3.11), the choice of $\|\mathbf{e}_{\mathbf{J}}\|_2$ as the cost function has the benefit of yielding a closed-form solution. However, in order to assess the rate of convergence, we must select a second norm that is used to report the error. $\|\mathbf{e}_{\mathbf{J}}\|_\infty$ is often preferred for error reporting in code verification because it is more sensitive and therefore more rigorous. However, the mismatch between the minimized norm (L^2) and the reported norm (L^∞) may require finer meshes to enter the asymptotic region. Therefore, as a trade-off, we additionally solve the optimization problem

$$\begin{aligned} &\text{minimize} && \|\mathbf{e}_{\mathbf{J}}\|_\infty \\ &\text{subject to} && a(\mathbf{J}_h, \mathbf{\Lambda}_i) = b\Big(\mathbf{E}^{\mathcal{I}}, \mathbf{H}^{\mathcal{I}}, \mathbf{\Lambda}_i\Big). \end{aligned} \tag{3.12}$$

The L^∞-norm of the error arising from the solution to (3.12) reaches the asymptotic region faster than that arising from (3.11) but requires the solution to a linear programming problem, which is more expensive.

3.4. Numerical-Integration Error

In practice, the integrals in $a(\cdot,\cdot)$ (2.19) and $b(\cdot,\cdot,\cdot)$ (2.20) are evaluated numerically, yielding the approximations $a^q(\cdot,\cdot)$ and $b^q(\cdot,\cdot,\cdot)$. $a^q(\cdot,\cdot)$ and $b^q(\cdot,\cdot,\cdot)$ are obtained by integrating over each triangular element using quadrature, and generally incur a numerical-integration error. Therefore, it is important to measure the numerical-integration error without contamination from the solution-discretization error.

In [54], approaches are presented to isolate the numerical-integration error by canceling or eliminating the solution-discretization error. In this report, we cancel the solution-discretization error and measure the numerical-integration error from

$$e_a = a^q(\mathbf{J}_{h_{\mathrm{MS}}}, \mathbf{J}_{h_{\mathrm{MS}}}) - a(\mathbf{J}_{h_{\mathrm{MS}}}, \mathbf{J}_{h_{\mathrm{MS}}}), \tag{3.13}$$

$$e_b = b^q\Big(\mathbf{E}^{\mathcal{I}}, \mathbf{H}^{\mathcal{I}}, \mathbf{J}_{h_{\mathrm{MS}}}\Big) - b\Big(\mathbf{E}^{\mathcal{I}}, \mathbf{H}^{\mathcal{I}}, \mathbf{J}_{h_{\mathrm{MS}}}\Big), \tag{3.14}$$

where $\mathbf{J}_{h_{\mathrm{MS}}}$ is the basis-function representation of $\mathbf{J}_{\mathrm{MS}}$, obtained from (2.21) by setting the coefficients J_j equal to the normal component of $\mathbf{J}_{\mathrm{MS}}$ at the midpoint of each edge associated with $\mathbf{\Lambda}_j(\mathbf{x})$. The presence of the basis functions in the minuend and subtrahend of (3.13) and (3.14) cancels the solution-discretization error. Equations (3.13) and (3.14) have the properties $|e_a| \leq C_a h^{p_a}$ and $|e_b| \leq C_b h^{p_b}$, where C_a and C_b are functions of the integrand derivatives, and p_a and p_b depend on the quadrature accuracy.

Reference [54] shows that e_a (3.13) and e_b (3.14) are proportional to their influence on the discretization error $\mathbf{e}_{\mathbf{J}}$ (3.10).

4. NUMERICAL EXAMPLES

In this chapter, we demonstrate the effectiveness of the approaches described in Chapter 3 using Gemma.

4.1. The Electric-Field Integral Equation

For the EFIE, we consider two unit-square flat plates, as shown in Figure 4-1, with one rotated out of the plane of the other by an angle θ.

We manufacture the surface current on the plate $\mathbf{J}_{\mathrm{MS}}(\mathbf{x}) = \{J_\xi(\boldsymbol{\xi}),\, J_\eta(\boldsymbol{\xi})\}$ using sinusoidal functions:

$$J_\xi(\boldsymbol{\xi}) = J_0 \cos(\pi\xi/2)\cos(\pi\eta/4), \tag{4.1}$$
$$J_\eta(\boldsymbol{\xi}) = J_0 \cos(\pi\xi/4)\sin(\pi\eta), \tag{4.2}$$

where $J_0 = 1$ A/m and the plate-fixed coordinate system $\boldsymbol{\xi}(\mathbf{x};\theta)$ is given by

$$\xi(\mathbf{x};\theta) = \frac{1}{L}\begin{cases} x, & \text{for } x \le 0 \text{ m} \\ x\cos\theta + z\sin\theta, & \text{for } x > 0 \text{ m} \end{cases},$$
$$\eta(\mathbf{x}) = y/L,$$

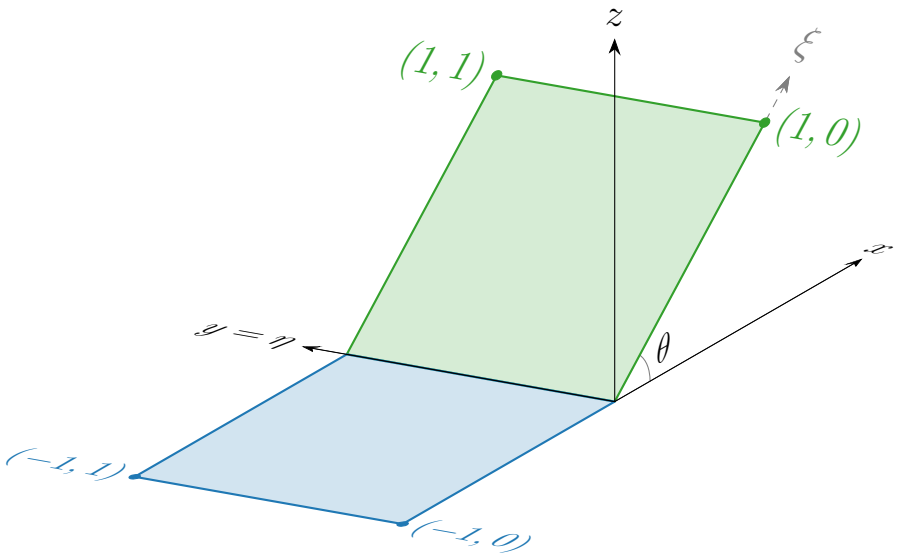

Figure 4-1. Computational domain consisting of two unit-square plates. Coordinates are expressed in the plate-fixed coordinate system $\boldsymbol{\xi}(\mathbf{x};\theta)$.

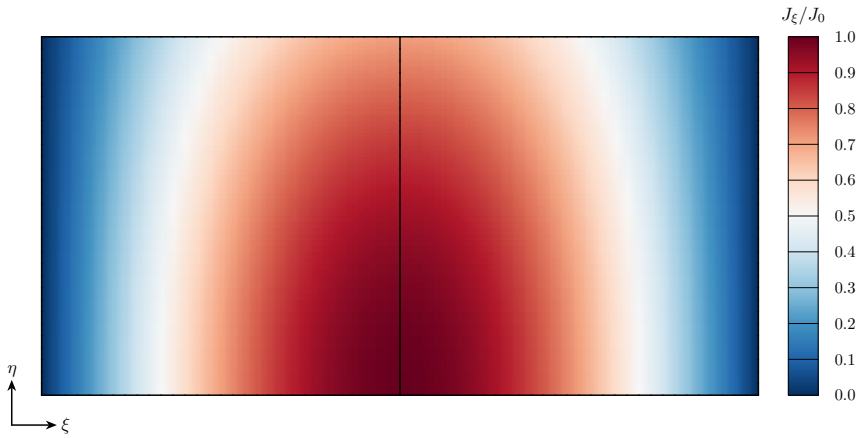

(a) J_ξ

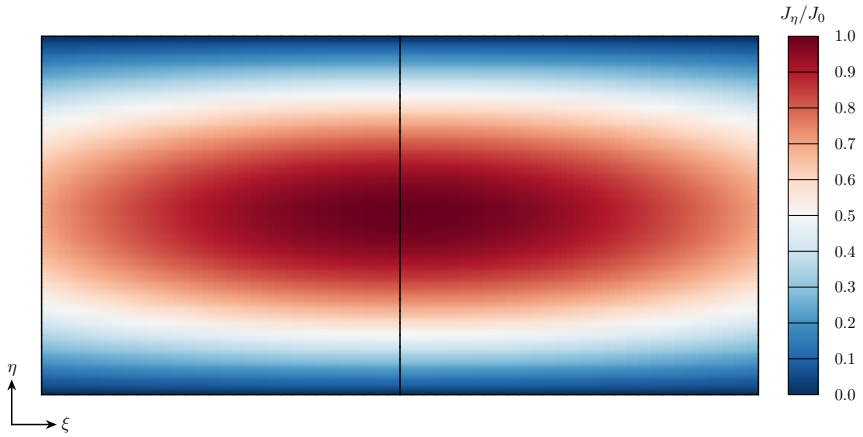

(b) J_η

Figure 4-2. Manufactured surface current $\mathbf{J}_{\text{MS}}$ for flat plates.

where $L = 1$ m. At the edges of the domain, the normal component of $\mathbf{J}_{\text{MS}}(\mathbf{x})$ is zero, satisfying the boundary conditions. Figures 4-2a and 4-2b provide plots of (4.1) and (4.2).

We consider two types of meshes: a uniform mesh and a twisted mesh, examples of which are shown in Figures 4-3a and 4-3b with the total number of triangles $n_t = 1600$. The twisted mesh is obtained by transforming the uniform mesh, using the transformation provided in Reference [28].

We account for potential disparities in the magnitudes of the contributions to $\mathbf{Z}$ from $\mathbf{A}$ and Φ:

$$\mathbf{Z} = \mathbf{Z}^{\mathbf{A}} + \mathbf{Z}^{\Phi},$$

where $Z^{\mathbf{A}}_{i,j} = a^{\mathbf{A}}(\mathbf{\Lambda}_j, \mathbf{\Lambda}_i)$ and $Z^{\Phi}_{i,j} = a^{\Phi}(\mathbf{\Lambda}_j, \mathbf{\Lambda}_i)$. To ensure the errors of one are not overshadowed by those of the other, we consider the contributions $\mathbf{Z}^{\mathbf{A}}$ and $\mathbf{Z}^{\Phi}$ together and separately, with $\epsilon = 1$ F/m and $\mu = 1$ H/m. $\mathbf{Z}^{\mathbf{A}}$ contains the factor $\omega\mu = k^2/(\epsilon\omega)$, whereas $\mathbf{Z}^{\Phi}$ contains the factor $1/(\epsilon\omega)$. When we consider the contributions separately, we are effectively taking

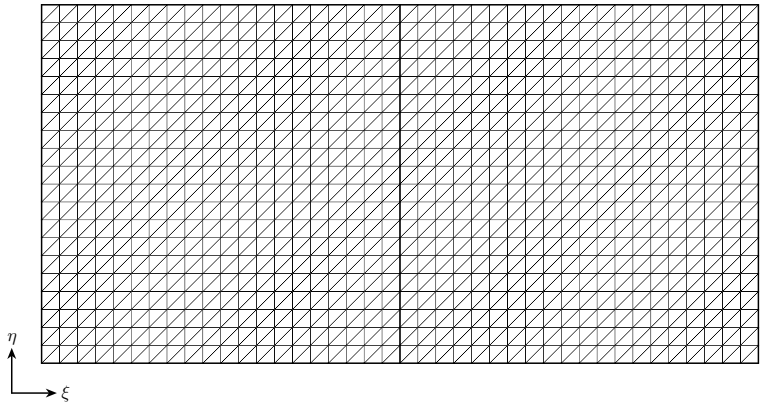

(a) Uniform

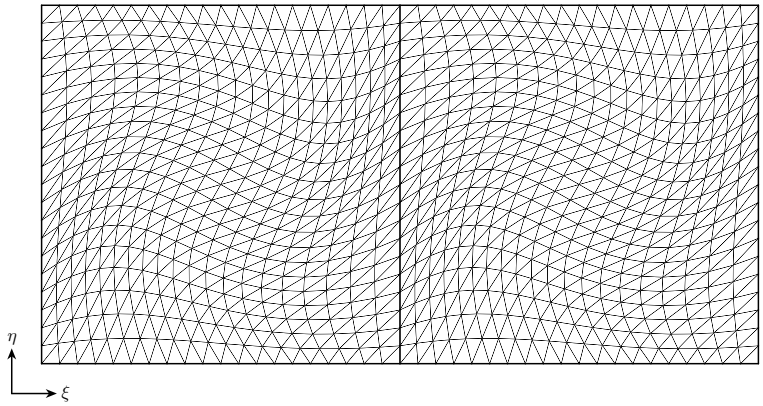

(b) Twisted

Figure 4-3. Two different types of meshes, shown with $n_t = 1600$.

the limits as $k \to \infty$ for $\mathbf{Z}^{\mathbf{A}}$ and $k \to 0$ for $\mathbf{Z}^{\Phi}$. When we consider the contributions together, we set $k = 1$ m^{-1} for $\mathbf{Z}$. We adjust $\mathbf{V}$ accordingly.

The numerical integration is performed using polynomial quadrature rules for triangles. For multiple quadrature point amounts, Table 4-1 lists the maximum polynomial degree of the integrand the points can integrate exactly [63, 64], as well as the convergence rates of the errors for inexact integrations of nonsingular integrands. These properties correspond to the optimal point locations and weights.

Number of points	1	3	4	6	7	12	13
Maximum integrand degree	1	2	3	4	5	6	7
Convergence rate	$\mathcal{O}(h^2)$	$\mathcal{O}(h^4)$	$\mathcal{O}(h^4)$	$\mathcal{O}(h^6)$	$\mathcal{O}(h^6)$	$\mathcal{O}(h^8)$	$\mathcal{O}(h^8)$

Table 4-1. Polynomial triangle quadrature properties.

4.1.1. Solution-Discretization Error

To isolate and measure the solution-discretization error, we proceed with the assessment described in Section 3.2. With G_{MS} (3.9), we are able to compute the integral in (3.7) analytically, which yields a finite-degree polynomial integrand for $b\Big(\mathbf{E}^{\mathcal{I}}, \mathbf{H}^{\mathcal{I}}, \mathbf{\Lambda}_i\Big)$ (2.22). Because the integrands of $a(\mathbf{J}_h, \mathbf{\Lambda}_i)$ and $b\Big(\mathbf{E}^{\mathcal{I}}, \mathbf{H}^{\mathcal{I}}, \mathbf{\Lambda}_i\Big)$ in (2.22) are finite-degree polynomials, they can be integrated exactly with the appropriate amount of polynomial quadrature points.

Figures 4-4 and 4-5 show the L^∞ norm of the discretization error $\|\mathbf{e_J}\|_\infty$ (3.10) arising from only the solution-discretization error for $\theta = \{0°, 45°, 90°, 135°\}$, $q = \{1, 2\}$ in G_{MS} (3.9), the uniform and twisted meshes, and the contributions to the EFIE together and separately. With G_{MS}, the matrices are practically singular; therefore, we use the approach of (3.11) in Section 3.3 to select a unique solution. The convergence rates are all $\mathcal{O}(h^2)$ as expected.

4.1.2. Numerical-Integration Error

To isolate and measure the numerical-integration error, we perform the assessments described in Section 3.4. Figures 4-6 and 4-7 show the numerical-integration errors e_a (3.13) and e_b (3.14) when the solution-discretization error is canceled for $\theta = \{0°, 135°\}$, $q = 2$ in G_{MS} (3.9), the twisted mesh, and the contributions to the EFIE together and separately. In the legend entries of the subfigures in the left columns of Figures 4-6 and 4-7, the first number is the amount of quadrature points used to compute the integral over S, whereas the second is the amount used to compute the integral over S'. In the legend entries of the subfigures in the right columns of Figures 4-6 and 4-7, the number is the amount of quadrature points used to compute the integral over S. The numerical-integration error is nondimensionalized by the constant $\varepsilon_0 = 1$ A·V. Each of the solutions converges at the expected rate listed in Table 4-1.

4.2. The Magnetic-Field Integral Equation

For the MFIE, we consider two domains: a cube and a rhombic prism, each with all edges of length 1 m, as shown in Figures 4-8 and 4-9 with the total number of triangles $n_t = 1200$. The acute angle of the rhombic prism is 45°. We manufacture the surface current density $\mathbf{J}_{\text{MS}}(\mathbf{x}) = J_\xi(\xi, \eta)\mathbf{e}_\xi$, where

$$J_\xi(\xi, \eta) = J_0 \begin{cases} \sin\left(\dfrac{\pi\xi}{2L}\right)\sin^3\left(\dfrac{\pi\eta}{L}\right), & \text{for } \mathbf{n}\cdot\mathbf{e}_y = 0 \\ 0, & \text{for } \mathbf{n}\cdot\mathbf{e}_y \neq 0 \end{cases}, \tag{4.3}$$

$J_0 = 1$ A/m, and $L = 1$ m. $\xi \in [0, 4]$ m is perpendicular to $\eta = y \in [0, 1]$ m, wrapping around the surfaces for which $\mathbf{n}\cdot\mathbf{e}_y = 0$, beginning at $x = 0$ m and $z = 1$ m for the cube and $x = z = \sqrt{2}/2$ m for the rhombic prism, as depicted in Figure 4-9, which shows the nets of these domains. Equation (4.3) is of class C^2. Figures 4-10 and 4-11 show plots of (4.3).

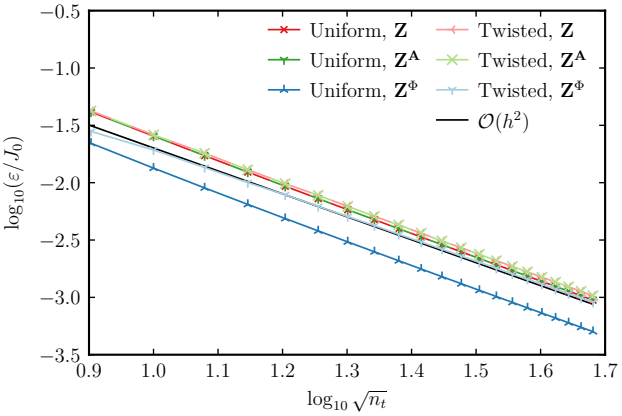

(a) $\theta = 0°$

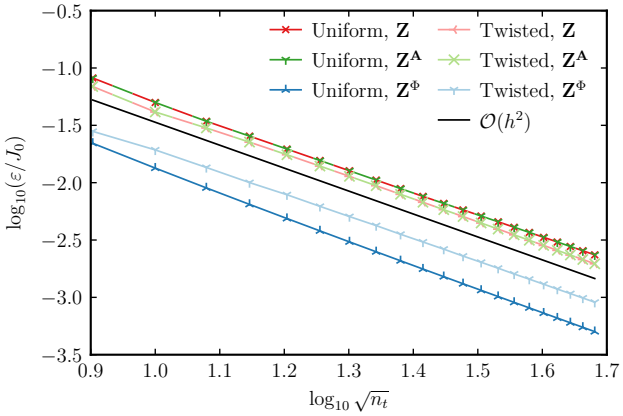

(b) $\theta = 45°$

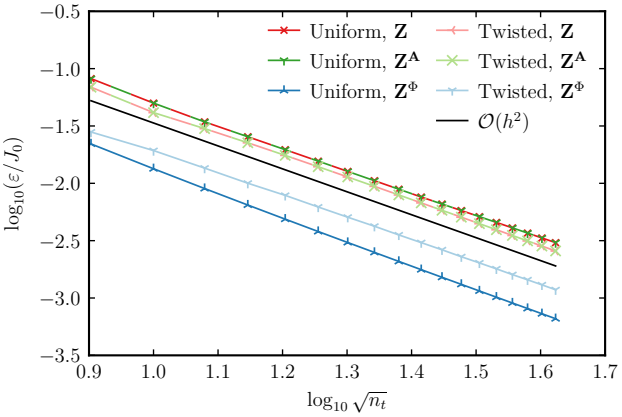

(c) $\theta = 90°$

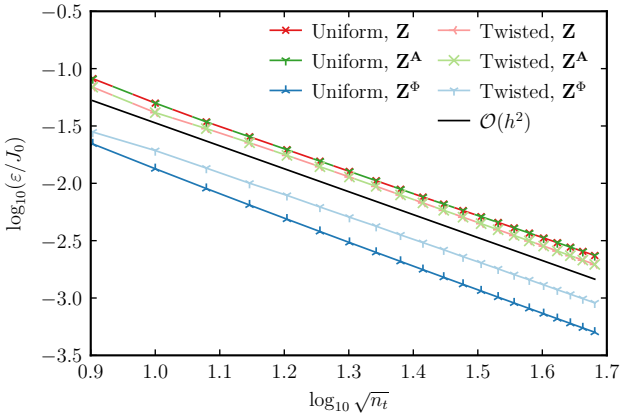

(d) $\theta = 135°$

Figure 4-4. EFIE, solution-discretization error: $\varepsilon = \|\mathbf{e}\|_\infty$ for $q = 1$ in G_{MS} (3.9).

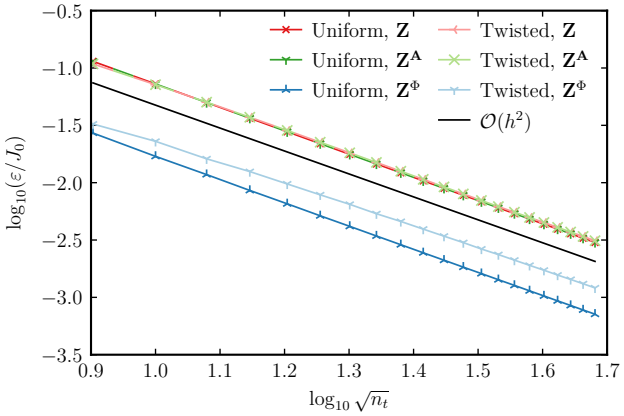

(a) $\theta = 0°$

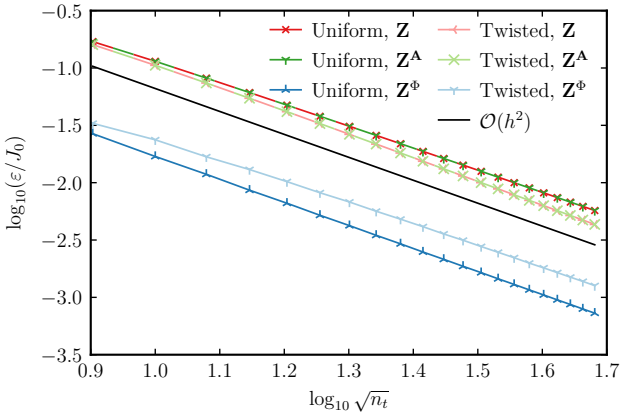

(b) $\theta = 45°$

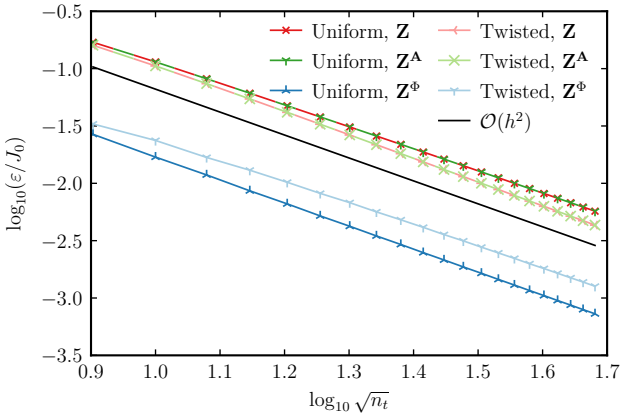

(c) $\theta = 90°$

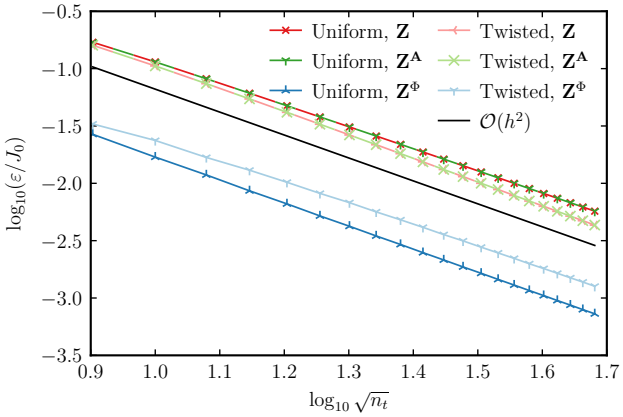

(d) $\theta = 135°$

Figure 4-5. EFIE, solution-discretization error: $\varepsilon = \|\mathbf{e}\|_\infty$ for $q = 2$ in G_{MS} (3.9).

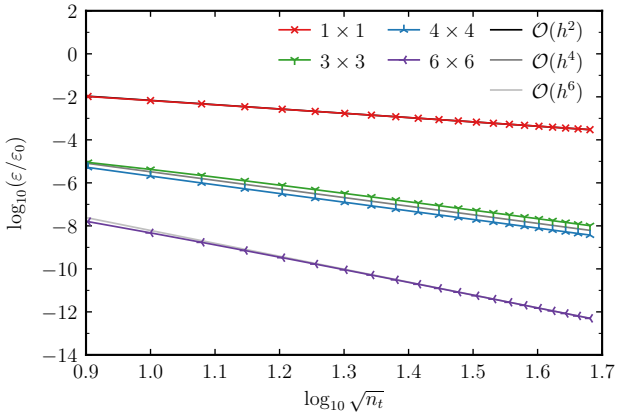

(a) $\mathbf{Z}$, $\varepsilon = |e_a|$ (3.13)

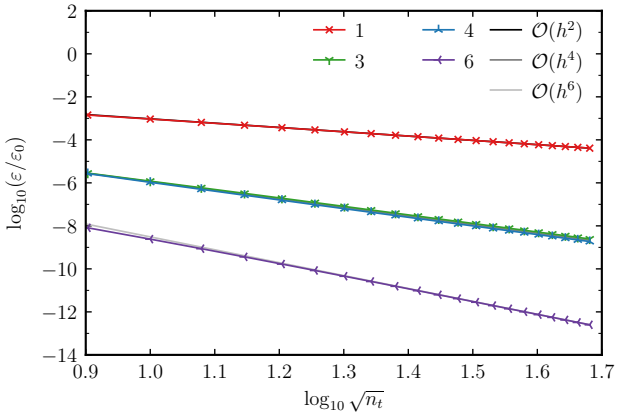

(b) $\mathbf{Z}$, $\varepsilon = |e_b|$ (3.14)

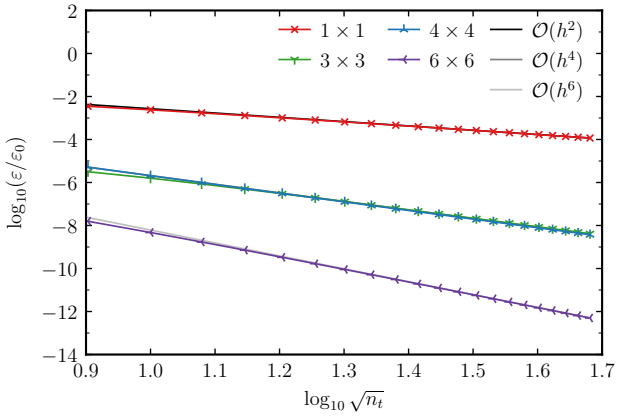

(c) $\mathbf{Z}^{\mathbf{A}}$, $\varepsilon = |e_a|$ (3.13)

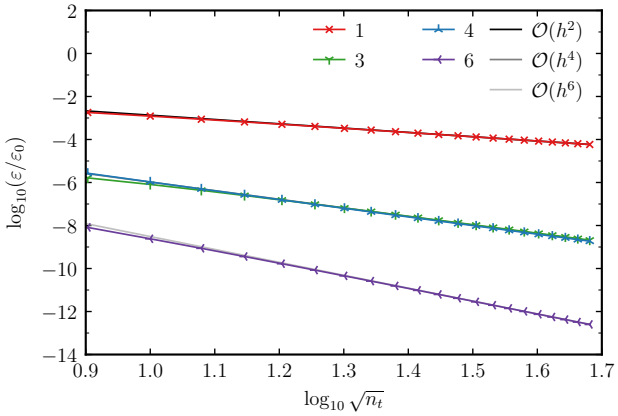

(d) $\mathbf{Z}^{\mathbf{A}}$, $\varepsilon = |e_b|$ (3.14)

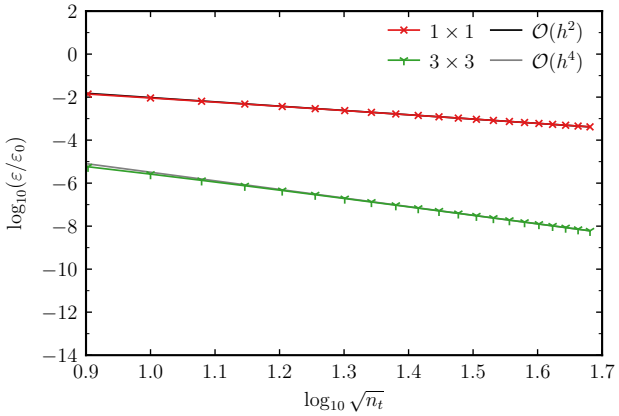

(e) $\mathbf{Z}^{\Phi}$, $\varepsilon = |e_a|$ (3.13)

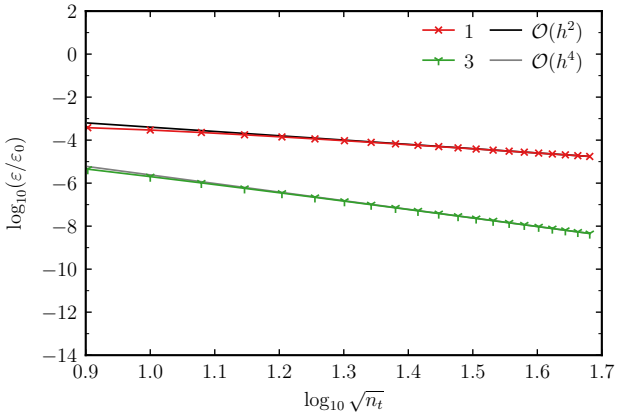

(f) $\mathbf{Z}^{\Phi}$, $\varepsilon = |e_b|$ (3.14)

Figure 4-6. EFIE, numerical-integration error: $q = 2$ in G_{MS} (3.9), $\theta = 0°$, twisted mesh.

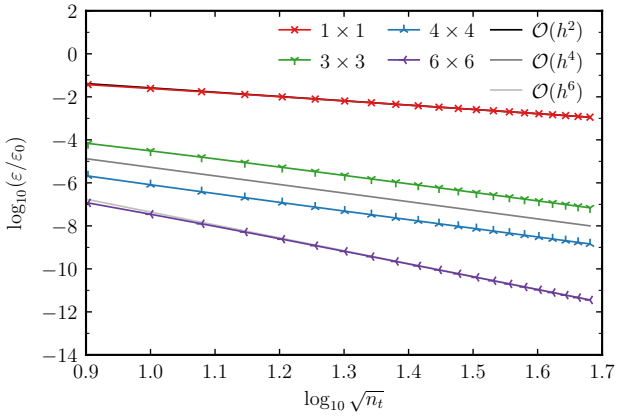

(a) $\mathbf{Z}$, $\varepsilon = |e_a|$ (3.13)

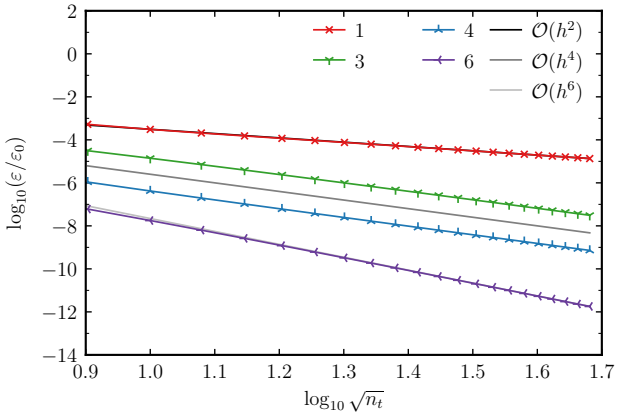

(b) $\mathbf{Z}$, $\varepsilon = |e_b|$ (3.14)

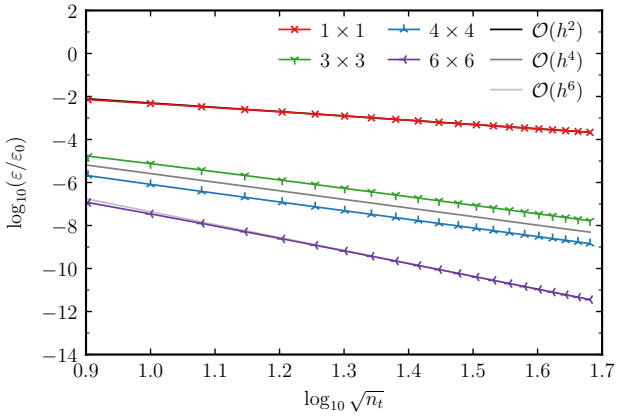

(c) $\mathbf{Z}^{\mathbf{A}}$, $\varepsilon = |e_a|$ (3.13)

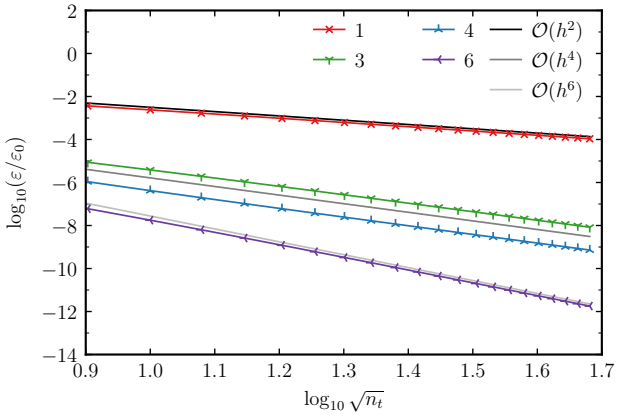

(d) $\mathbf{Z}^{\mathbf{A}}$, $\varepsilon = |e_b|$ (3.14)

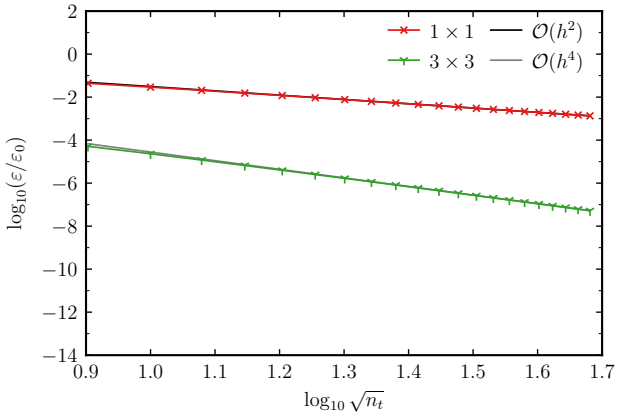

(e) $\mathbf{Z}^{\Phi}$, $\varepsilon = |e_a|$ (3.13)

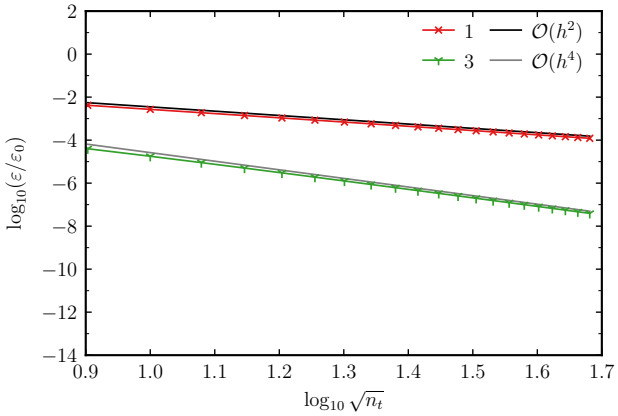

(f) $\mathbf{Z}^{\Phi}$, $\varepsilon = |e_b|$ (3.14)

Figure 4-7. EFIE, numerical-integration error: $q = 2$ in G_{MS} (3.9), $\theta = 135°$, twisted mesh.

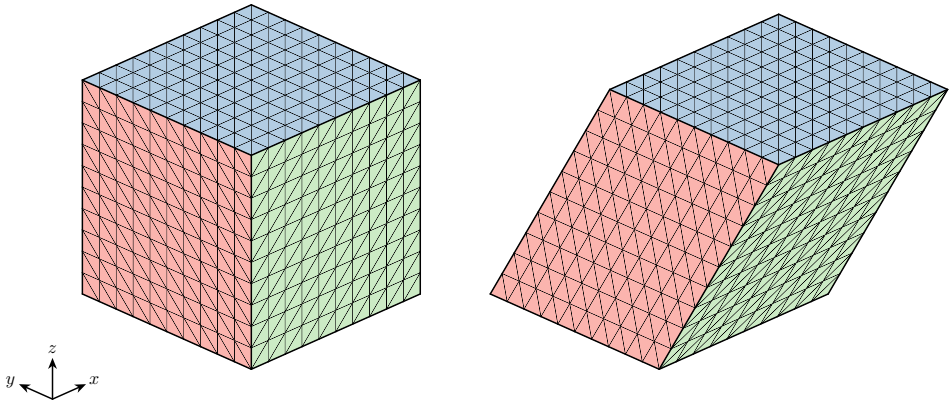

Figure 4-8. Meshes for the cube (left) and the rhombic prism (right), with $n_t = 1200$.

We account for potential disparities in the magnitudes of the contributions to (2.17) from the first (Term 1) and second (Term 2) terms by considering them together and separately.

4.2.1. Solution-Discretization Error

To isolate and measure the solution-discretization error, we proceed with the assessment described in Section 3.2. With G_{MS} (3.9), we are able to compute the integral in (3.8) analytically, which yields a finite-degree polynomial integrand for $b\Big(\mathbf{E}^{\mathcal{I}}, \mathbf{H}^{\mathcal{I}}, \mathbf{\Lambda}_i\Big)$ (2.22). Because the integrands of $a(\mathbf{J}_h, \mathbf{\Lambda}_i)$ and $b\Big(\mathbf{E}^{\mathcal{I}}, \mathbf{H}^{\mathcal{I}}, \mathbf{\Lambda}_i\Big)$ in (2.22) are finite-degree polynomials, they can be integrated exactly with the appropriate amount of polynomial quadrature points.

Figure 4-12 shows the L^∞ norm of the discretization error $\|\mathbf{e_J}\|_\infty$ (3.10) arising from only the solution-discretization error for the cube and rhombic prism for $q = \{1, 2\}$ in G_{MS} (3.9). For Term 1 and both terms, the matrices are nonsingular, and the convergence rates are all $\mathcal{O}(h^2)$ as expected. With G_{MS}, the matrices for Term 2 are practically singular; therefore, we use the approaches of (3.11) and (3.12) in Section 3.3 to select unique solutions. Minimizing $\|\mathbf{e_J}\|_\infty$ (3.12) yields lower error values that approach $\mathcal{O}(h^2)$ sooner.

4.2.2. Numerical-Integration Error

To isolate and measure the numerical-integration error, we perform the assessments described in Section 3.4. Figure 4-13 shows the numerical-integration errors e_a (3.13) and e_b (3.14) when the solution-discretization error is canceled for the cube and rhombic prism with $q = 2$ in G_{MS} (3.9). In the legend entries of the subfigures in the left column of Figure 4-13, the first number is the amount of quadrature points used to compute the integral over S, whereas the second is the amount used to compute the integral over S'. In the legend entries of the subfigures in the right column of Figure 4-13, the number is the amount of quadrature points used to compute the integral over S. The numerical-integration error is nondimensionalized

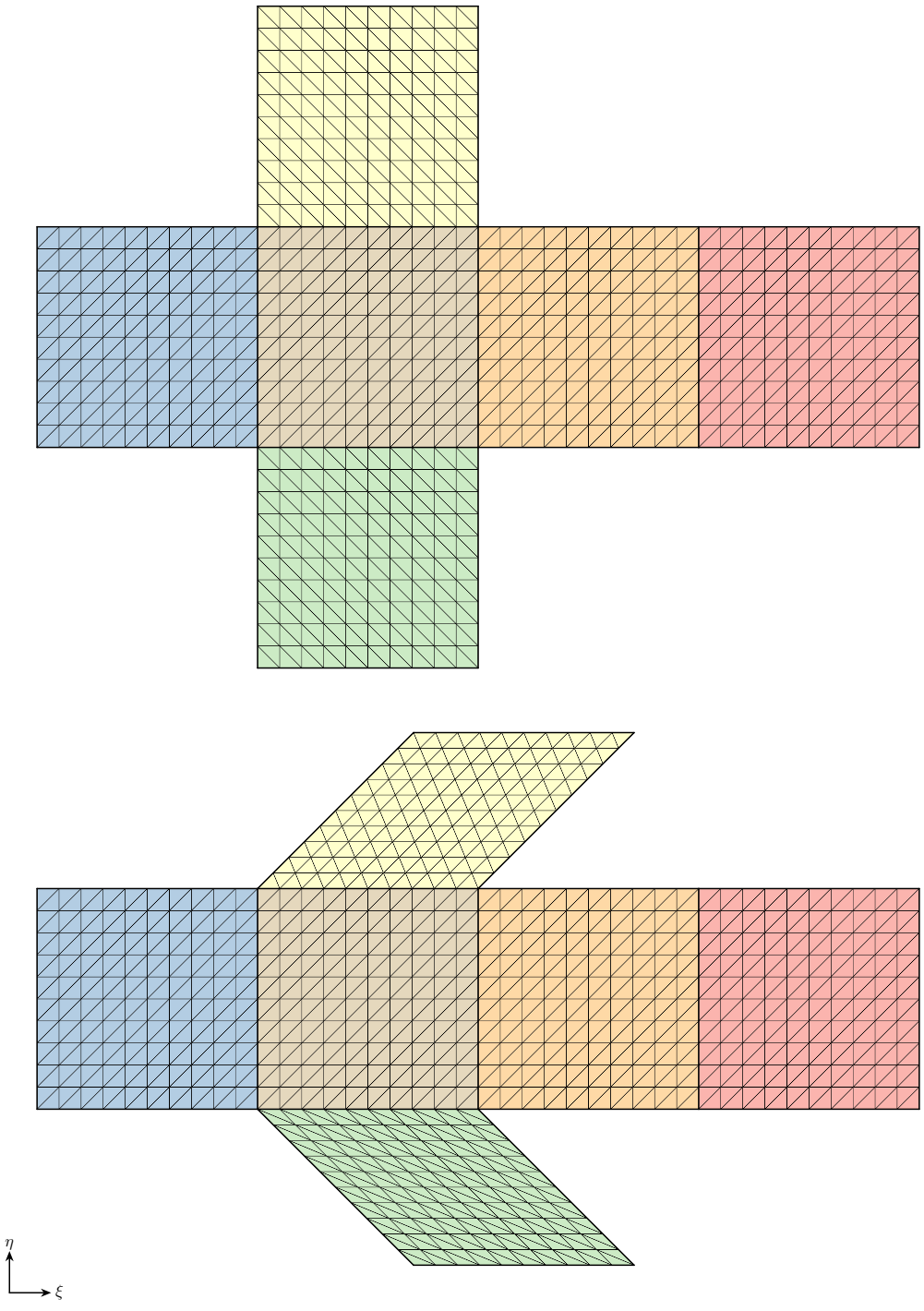

Figure 4-9. Meshes for the cube (top) and the rhombic prism (bottom), with $n_t = 1200$.

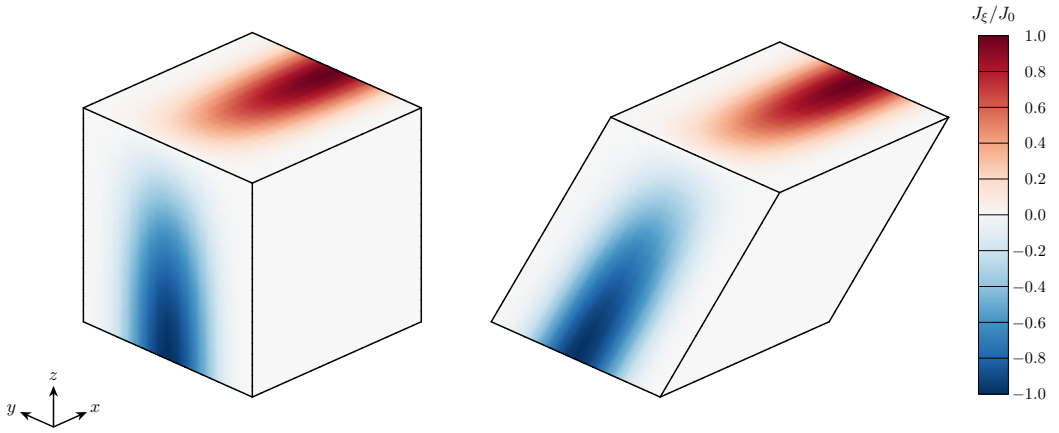

Figure 4-10. Manufactured surface current density $\mathbf{J}_{\mathrm{MS}}$ for the cube (left) and the rhombic prism (right).

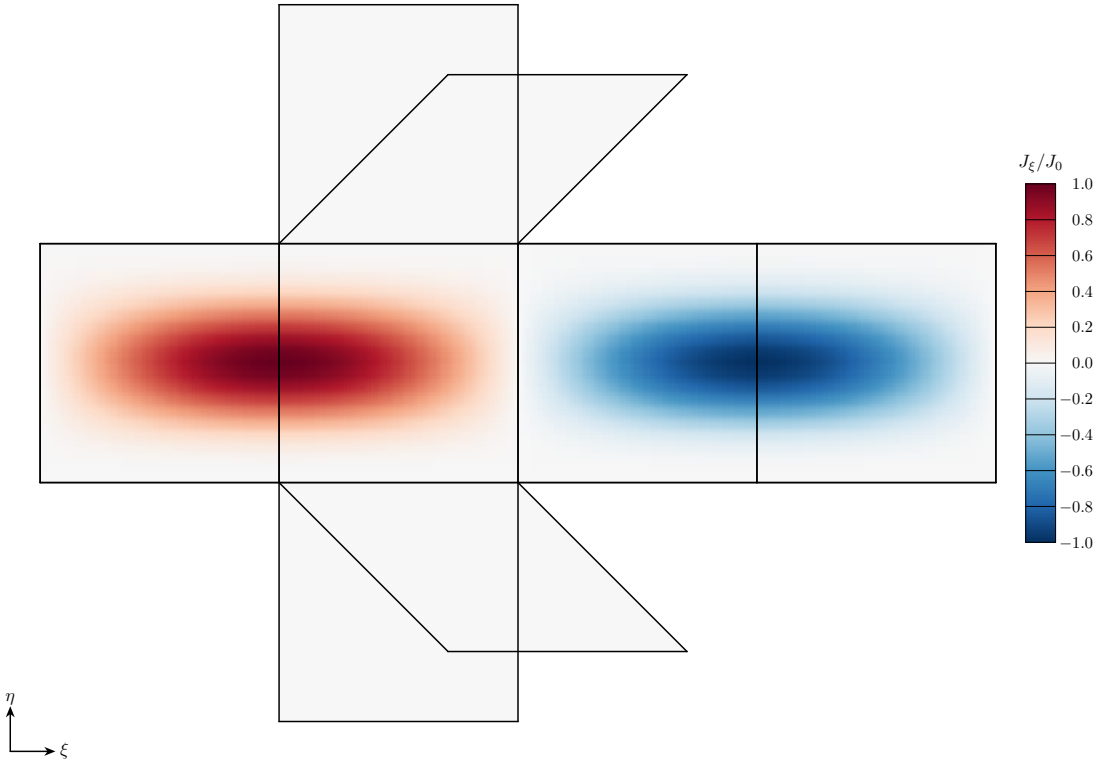

Figure 4-11. Manufactured surface current density $\mathbf{J}_{\mathrm{MS}}$ for cube and rhombic prism.

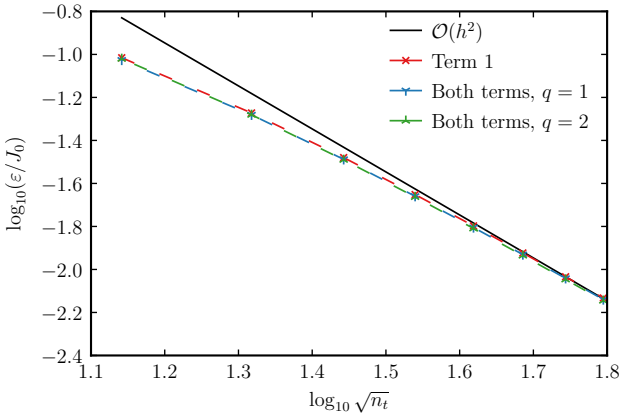

(a) Cube, Term 1 and both terms

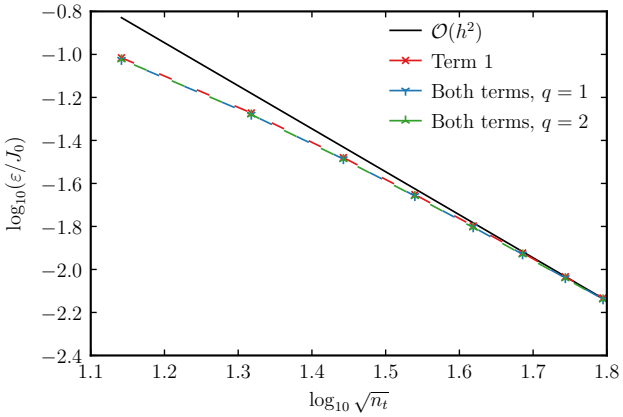

(b) Rhombic prism, Term 1 and both terms

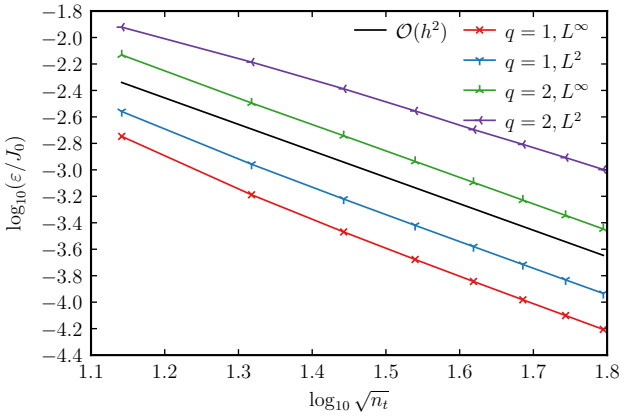

(c) Cube, Term 2

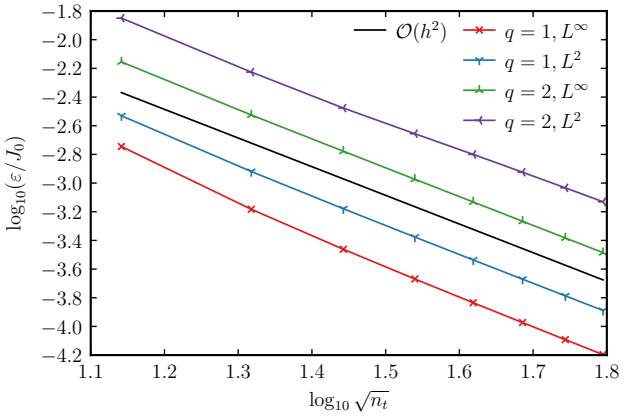

(d) Rhombic prism, Term 2

Figure 4-12. MFIE, solution-discretization error: $\varepsilon = \|\mathbf{e}\|_\infty$ for different term combinations and q values in G_{MS} (3.9). For Term 2, a unique solution is obtained by minimizing $\|\mathbf{e_J}\|_2$ (3.11) and $\|\mathbf{e_J}\|_\infty$ (3.12).

by the constant $\varepsilon_0 = 1$ A^2. Each of the solutions converges at the expected rate listed in Table 4-1.

4.3. The Combined-Field Integral Equation

For the CFIE, we consider the cube and rhombic prism from Section 4.2.

4.3.1. Solution-Discretization Error

To isolate and measure the solution-discretization error, we proceed with the assessment described in Section 3.2. With G_{MS} (3.9), we are able to compute the integral in (3.8) analytically, which yields a finite-degree polynomial integrand for $b\left(\mathbf{E}^{\mathcal{I}}, \mathbf{H}^{\mathcal{I}}, \mathbf{\Lambda}_i\right)$ (2.22). Because

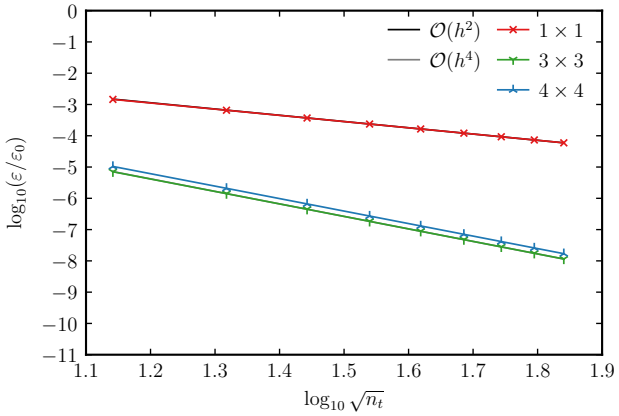

(a) Cube, $\varepsilon = |e_a|$ (3.13)

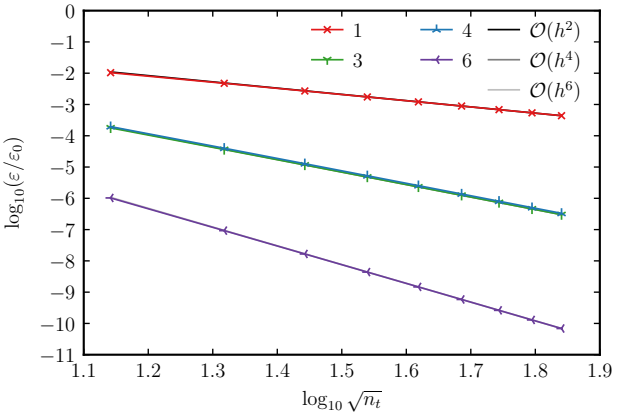

(b) Cube, $\varepsilon = |e_b|$ (3.14)

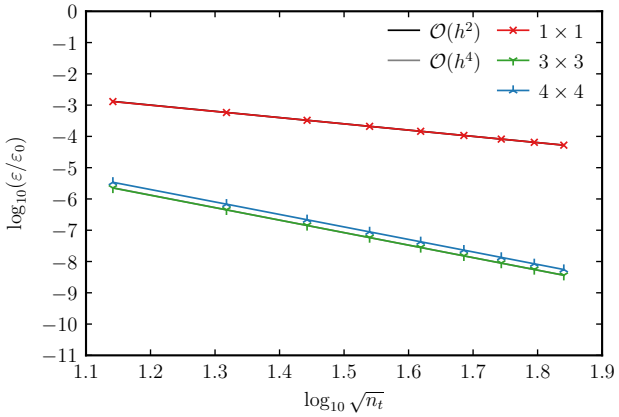

(c) Rhombic prism, $\varepsilon = |e_a|$ (3.13)

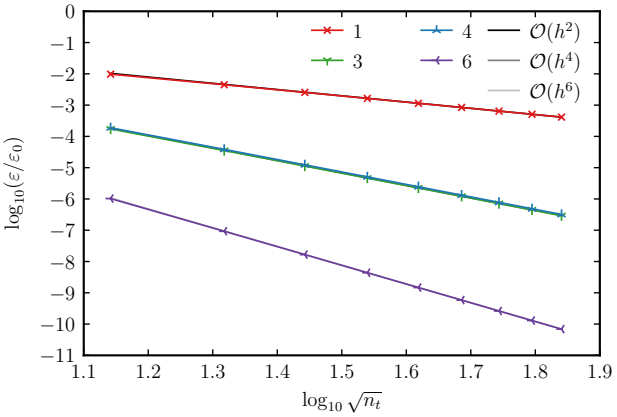

(d) Rhombic prism, $\varepsilon = |e_b|$ (3.14)

Figure 4-13. MFIE, numerical-integration error: $q = 2$ in G_{MS} (3.9).

the integrands of $a(\mathbf{J}_h, \mathbf{\Lambda}_i)$ and $b\Big(\mathbf{E}^{\mathcal{I}}, \mathbf{H}^{\mathcal{I}}, \mathbf{\Lambda}_i\Big)$ in (2.22) are finite-degree polynomials, they can be integrated exactly with the appropriate amount of polynomial quadrature points.

For multiple values of the combination parameter α, Figure 4-14 shows the L^∞ norm of the discretization error $\|\mathbf{e}_\mathbf{J}\|_\infty$ (3.10) arising from only the solution-discretization error for the cube and rhombic prism for $q = \{1, 2\}$ in G_{MS} (3.9). The matrices are nonsingular. The convergence rates are all $\mathcal{O}(h^2)$ as expected.

4.3.2. Numerical-Integration Error

To isolate and measure the numerical-integration error, we perform the assessments described in Section 3.4. Figure 4-15 shows the numerical-integration errors e_a (3.13) and e_b (3.14) when the solution-discretization error is canceled for the cube and rhombic prism with $\alpha = 1/2$ and $q = 2$ in G_{MS} (3.9). In the legend entries of the subfigures in the left column of Figure 4-15, the first number is the amount of quadrature points used to compute the integral over S, whereas the second is the amount used to compute the integral over S'. In the legend entries of the subfigures in the right column of Figure 4-15, the number is the amount of quadrature points used to compute the integral over S. The numerical-integration error is nondimensionalized by the constant $\varepsilon_0 = 1$ A^2. Each of the solutions converges at the expected rate listed in Table 4-1.

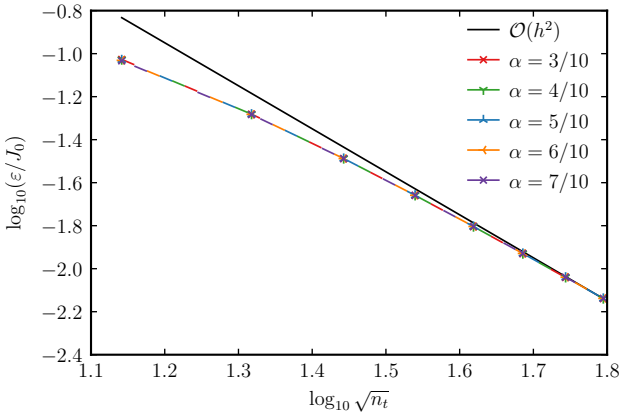

(a) Cube, $q = 1$ in G_{MS} (3.9)

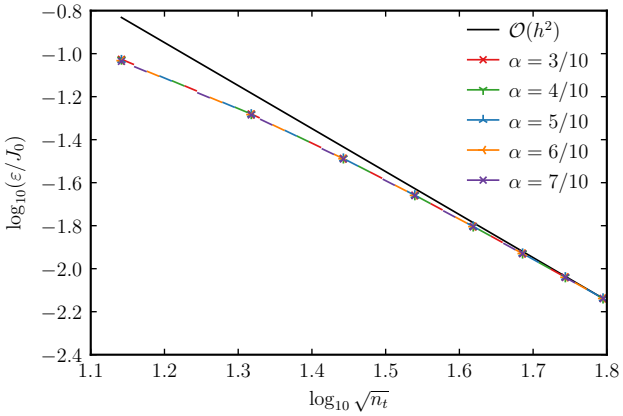

(b) Rhombic prism, $q = 1$ in G_{MS} (3.9)

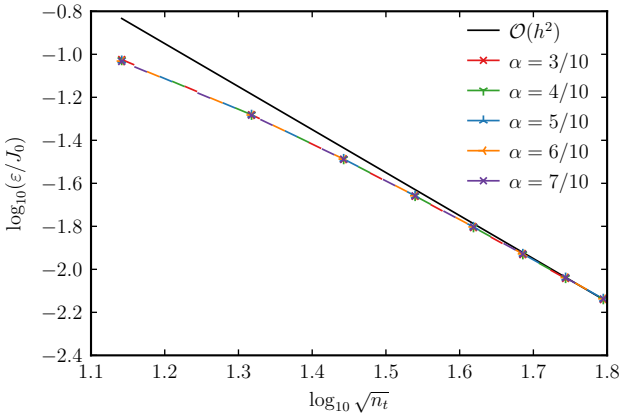

(c) Cube, $q = 2$ in G_{MS} (3.9)

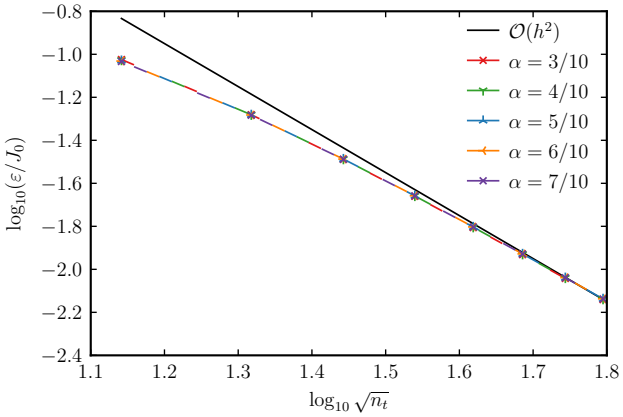

(d) Rhombic prism, $q = 2$ in G_{MS} (3.9)

Figure 4-14. CFIE, solution-discretization error: $\varepsilon = \|\mathbf{e}\|_\infty$ for different combination parameters α.

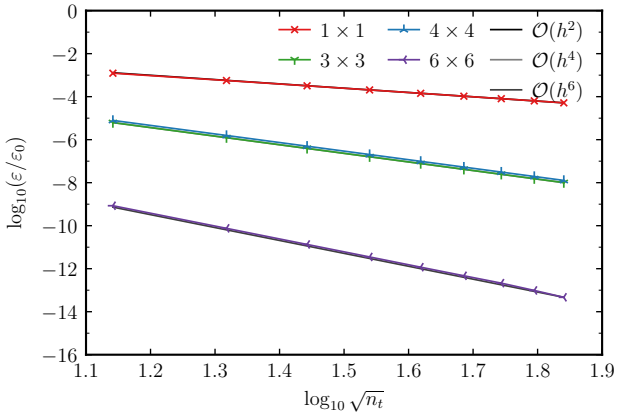

(a) Cube, $\varepsilon = |e_a|$ (3.13)

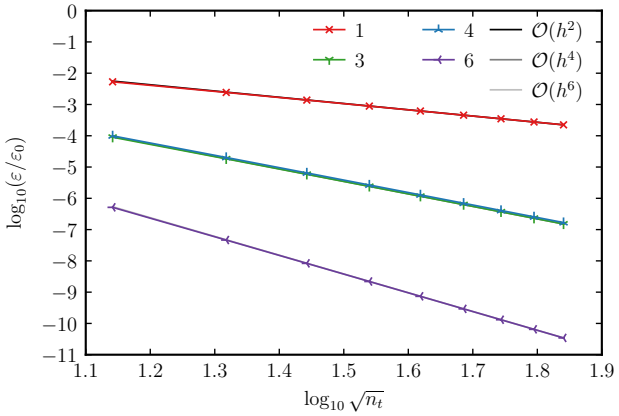

(b) Cube, $\varepsilon = |e_b|$ (3.14)

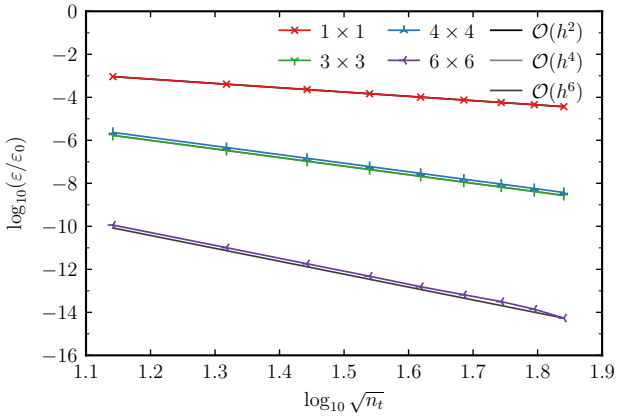

(c) Rhombic prism, $\varepsilon = |e_a|$ (3.13)

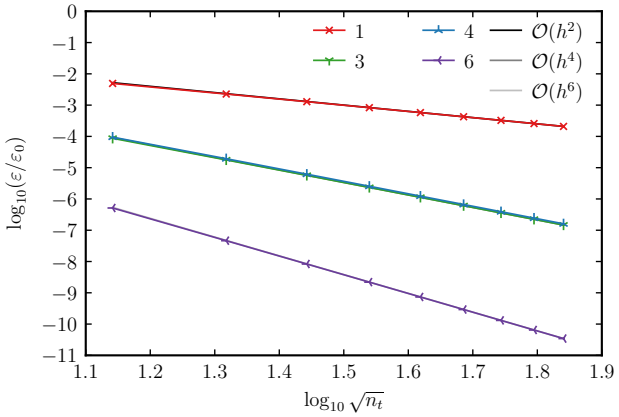

(d) Rhombic prism, $\varepsilon = |e_b|$ (3.14)

Figure 4-15. CFIE, numerical-integration error: $\alpha = 1/2$, $q = 2$ in G_{MS} (3.9).

5. CONCLUSIONS

In this report, we presented code-verification approaches for the method-of-moments implementation of the electric-, magnetic, and combined-field integral equations to isolate and measure the solution-discretization error and numerical-integration error in Gemma.

We isolated and measured the solution-discretization error by integrating exactly over the domain. To integrate exactly, we manufactured the Green's function, and presented optimization approaches to select a unique solution when the manufactured Green's function makes the matrix practically singular.

We isolated and measured the numerical-integration error by removing the solution-discretization error. We removed the solution-discretization error by canceling the basis-function contribution.

We demonstrated the efficacy of these approaches and observed the expected rates of convergence from Gemma.

This report underscores the critical role of rigorous code verification in ensuring the reliability and accuracy of computational electromagnetics solutions, paving the way for Gemma to contribute significantly to advancements in the field and inspire further research into innovative verification methodologies.

REFERENCES

[1] R. D. Graglia, On the numerical integration of the linear shape functions times the 3-D Green's function or its gradient on a plane triangle, IEEE Transactions on Antennas and Propagation 41 (10) (1993) 1448–1455. doi:10.1109/8.247786.

[2] D. Wilton, S. Rao, A. Glisson, D. Schaubert, O. Al-Bundak, C. Butler, Potential integrals for uniform and linear source distributions on polygonal and polyhedral domains, IEEE Transactions on Antennas and Propagation 32 (3) (1984) 276–281. doi:10.1109/TAP.1984.1143304.

[3] S. Rao, D. Wilton, A. Glisson, Electromagnetic scattering by surfaces of arbitrary shape, IEEE Transactions on Antennas and Propagation 30 (3) (1982) 409–418. doi:10.1109/TAP.1982.1142818.

[4] M. A. Khayat, D. R. Wilton, Numerical evaluation of singular and near-singular potential integrals, IEEE Transactions on Antennas and Propagation 53 (10) (2005) 3180–3190. doi:10.1109/TAP.2005.856342.

[5] P. W. Fink, D. R. Wilton, M. A. Khayat, Simple and efficient numerical evaluation of near-hypersingular integrals, IEEE Antennas and Wireless Propagation Letters 7 (2008) 469–472. doi:10.1109/LAWP.2008.2000788.

[6] M. A. Khayat, D. R. Wilton, P. W. Fink, An improved transformation and optimized sampling scheme for the numerical evaluation of singular and near-singular potentials, IEEE Antennas and Wireless Propagation Letters 7 (2008) 377–380. doi:10.1109/LAWP.2008.928461.

[7] F. Vipiana, D. R. Wilton, Optimized numerical evaluation of singular and near-singular potential integrals involving junction basis functions, IEEE Transactions on Antennas and Propagation 59 (1) (2011) 162–171. doi:10.1109/TAP.2010.2090464.

[8] F. Vipiana, D. R. Wilton, Numerical evaluation via singularity cancellation schemes of near-singular integrals involving the gradient of Helmholtz-type potentials, IEEE Transactions on Antennas and Propagation 61 (3) (2013) 1255–1265. doi:10.1109/TAP.2012.2227922.

[9] M. M. Botha, A family of augmented Duffy transformations for near-singularity cancellation quadrature, IEEE Transactions on Antennas and Propagation 61 (6) (2013) 3123–3134. doi:10.1109/TAP.2013.2252137.

[10] J. Rivero, F. Vipiana, D. R. Wilton, W. A. Johnson, Hybrid integration scheme for the evaluation of strongly singular and near-singular integrals in surface integral equations, IEEE Transactions on Antennas and Propagation 67 (10) (2019). doi:10.1109/TAP.2019.2920333.

[11] F. Vipiana, D. R. Wilton, W. A. Johnson, Advanced numerical schemes for the accurate evaluation of 4-D reaction integrals in the method of moments, IEEE Transactions on Antennas and Propagation 61 (11) (2013) 5559–5566. doi:10.1109/TAP.2013.2277864.

[12] A. G. Polimeridis, F. Vipiana, J. R. Mosig, D. R. Wilton, DIRECTFN: Fully numerical algorithms for high precision computation of singular integrals in Galerkin SIE methods, IEEE Transactions on Antennas and Propagation 61 (6) (2013) 3112–3122. doi:10.1109/TAP.2013.2246854.

[13] D. R. Wilton, F. Vipiana, W. A. Johnson, Evaluation of 4-D reaction integrals in the method of moments: Coplanar element case, IEEE Transactions on Antennas and Propagation 65 (5) (2017) 2479–2493. doi:10.1109/TAP.2017.2677916.

[14] J. Rivero, F. Vipiana, D. R. Wilton, W. A. Johnson, Evaluation of 4-D reaction integrals via double application of the divergence theorem, IEEE Transactions on Antennas and Propagation 67 (2) (2019) 1131–1142. doi:10.1109/TAP.2018.2882589.

[15] B. A. Freno, W. A. Johnson, B. F. Zinser, D. F. Wilton, F. Vipiana, S. Campione, Characterization and integration of the singular test integrals in the method-of-moments implementation of the electric-field integral equation, Engineering Analysis with Boundary Elements 124 (2021) 185–193. doi:10.1016/j.enganabound.2020.12.015.

[16] P. J. Roache, Verification and Validation in Computational Science and Engineering, Hermosa Publishers, 1998.

[17] P. Knupp, K. Salari, Verification of Computer Codes in Computational Science and Engineering, Chapman & Hall/CRC, 2002. doi:10.1201/9781420035421.

[18] W. L. Oberkampf, C. J. Roy, Verification and Validation in Scientific Computing, Cambridge University Press, 2010. doi:10.1017/cbo9780511760396.

[19] C. J. Roy, Review of code and solution verification procedures for computational simulation, Journal of Computational Physics 205 (1) (2005) 131–156. doi:10.1016/j.jcp.2004.10.036.

[20] P. J. Roache, Code verification by the method of manufactured solutions, Journal of Fluids Engineering 124 (1) (2001) 4–10. doi:10.1115/1.1436090.

[21] H. Nishikawa, Analytical formulas for verification of aerodynamic force and moment computations, Journal of Computational Physics 466 (2022). doi:10.1016/j.jcp.2022.111408.

[22] C. J. Roy, C. C. Nelson, T. M. Smith, C. C. Ober, Verification of Euler/Navier–Stokes codes using the method of manufactured solutions, International Journal for Numerical Methods in Fluids 44 (6) (2004) 599–620. doi:10.1002/fld.660.

[23] R. B. Bond, C. C. Ober, P. M. Knupp, S. W. Bova, Manufactured solution for computational fluid dynamics boundary condition verification, AIAA Journal 45 (9) (2007) 2224–2236. doi:10.2514/1.28099.

[24] S. Veluri, C. Roy, E. Luke, Comprehensive code verification for an unstructured finite volume CFD code, in: 48th AIAA Aerospace Sciences Meeting including the New Horizons Forum and Aerospace Exposition, American Institute of Aeronautics and Astronautics, 2010. doi:10.2514/6.2010-127.

[25] T. Oliver, K. Estacio-Hiroms, N. Malaya, G. Carey, Manufactured solutions for the Favre-averaged Navier–Stokes equations with eddy-viscosity turbulence models, in: 50th AIAA Aerospace Sciences Meeting including the New Horizons Forum and Aerospace Exposition, American Institute of Aeronautics and Astronautics, 2012. doi:10.2514/6.2012-80.

[26] L. Eça, C. M. Klaij, G. Vaz, M. Hoekstra, F. Pereira, On code verification of RANS solvers, Journal of Computational Physics 310 (2016) 418–439. doi:10.1016/j.jcp.2016.01.002.

[27] A. Hennink, M. Tiberga, D. Lathouwers, A pressure-based solver for low-Mach number flow using a discontinuous Galerkin method, Journal of Computational Physics 425 (2022). doi:10.1016/j.jcp.2020.109877.

[28] B. A. Freno, B. R. Carnes, V. G. Weirs, Code-verification techniques for hypersonic reacting flows in thermochemical nonequilibrium, Journal of Computational Physics 425 (2021). doi:10.1016/j.jcp.2020.109752.

[29] É. Chamberland, A. Fortin, M. Fortin, Comparison of the performance of some finite element discretizations for large deformation elasticity problems, Computers & Structures 88 (11) (2010) 664 – 673. doi:10.1016/j.compstruc.2010.02.007.

[30] S. Étienne, A. Garon, D. Pelletier, Some manufactured solutions for verification of fluid–structure interaction codes, Computers & Structures 106–107 (2012) 56–67. doi:10.1016/j.compstruc.2012.04.006.

[31] M. Bukač, G. Fu, A. Seboldt, C. Trenchea, Time-adaptive partitioned method for fluid–structure interaction problems with thick structures, Journal of Computational Physics 473 (2023). doi:10.1016/j.jcp.2022.111708.

[32] A. Veeraragavan, J. Beri, R. J. Gollan, Use of the method of manufactured solutions for the verification of conjugate heat transfer solvers, Journal of Computational Physics 307 (2016) 308–320. doi:10.1016/j.jcp.2015.12.004.

[33] P. T. Brady, M. Herrmann, J. M. Lopez, Code verification for finite volume multiphase scalar equations using the method of manufactured solutions, Journal of Computational Physics 231 (7) (2012) 2924–2944. doi:10.1016/j.jcp.2011.12.040.

[34] S. Lovato, S. L. Toxopeus, J. W. Settels, G. H. Keetels, G. Vaz, Code verification of non-Newtonian fluid solvers for single- and two-phase laminar flows, Journal of Verification, Validation and Uncertainty Quantification 6 (2) (2021). doi:10.1115/1.4050131.

[35] R. G. McClarren, R. B. Lowrie, Manufactured solutions for the p_1 radiation-hydrodynamics equations, Journal of Quantitative Spectroscopy and Radiative Transfer 109 (15) (2008) 2590–2602. doi:10.1016/j.jqsrt.2008.06.003.

[36] F. Riva, C. F. Beadle, P. Ricci, A methodology for the rigorous verification of particle-in-cell simulations, Physics of Plasmas 24 (2017). doi:10.1063/1.4977917.

[37] P. Tranquilli, L. Ricketson, L. Chacón, A deterministic verification strategy for electrostatic particle-in-cell algorithms in arbitrary spatial dimensions using the method of manufactured solutions, Journal of Computational Physics 448 (2022). doi:10.1016/j.jcp.2021.110751.

[38] A. M. Rueda-Ramírez, F. J. Hindenlang, J. Chan, G. J. Gassner, Entropy-stable Gauss collocation methods for ideal magneto-hydrodynamics, Journal of Computational Physics 475 (2023). doi:10.1016/j.jcp.2022.111851.

[39] J. Rudi, M. Heldman, E. M. Constantinescu, Q. Tang, X.-Z. Tang, Scalable implicit solvers with dynamic mesh adaptation for a relativistic drift-kinetic Fokker–Planck–Boltzmann model, Journal of Computational Physics 507 (2024). doi:10.1016/j.jcp.2024.112954.

[40] A. Amor-Martin, L. E. Garcia-Castillo, J.-F. Lee, Study of accuracy of a non-conformal finite element domain decomposition method, Journal of Computational Physics 429 (2021). doi:10.1016/j.jcp.2020.109989.

[41] A. J. Amar, B. F. Blackwell, J. R. Edwards, One-dimensional ablation using a full Newton's method and finite control volume procedure, Journal of Thermophysics and Heat Transfer 22 (1) (2008) 71–82. doi:10.2514/1.29610.

[42] A. J. Amar, B. F. Blackwell, J. R. Edwards, Development and verification of a one-dimensional ablation code including pyrolysis gas flow, Journal of Thermophysics and Heat Transfer 23 (1) (2009) 59–71. doi:10.2514/1.36882.

[43] A. Amar, N. Calvert, B. Kirk, Development and verification of the charring ablating thermal protection implicit system solver, in: 49th AIAA Aerospace Sciences Meeting including the New Horizons Forum and Aerospace Exposition, 2011. doi:10.2514/6.2011-144.

[44] B. A. Freno, B. R. Carnes, N. R. Matula, Nonintrusive manufactured solutions for ablation, Physics of Fluids 33 (1) (2021). doi:10.1063/5.0037245.

[45] B. A. Freno, B. R. Carnes, V. E. Brunini, N. R. Matula, Nonintrusive manufactured solutions for non-decomposing ablation in two dimensions, Journal of Computational Physics 463 (2022). doi:10.1016/j.jcp.2022.111237.

[46] R. G. Marchand, The method of manufactured solutions for the verification of computational electromagnetic codes, PhD dissertation, Stellenbosch University (Mar. 2013).

[47] R. G. Marchand, D. B. Davidson, Verification of the method-of-moment codes using the method of manufactured solutions, IEEE Transactions on Electromagnetic Compatibility 56 (4) (2014) 835–843. doi:10.1109/TEMC.2014.2325826.

[48] S. Adrian, F. Andriulli, T. Eibert, On a refinement-free Calderón multiplicative preconditioner for the electric field integral equation, Journal of Computational Physics 376 (2019) 1232–1252. doi:10.1016/j.jcp.2018.10.009.

[49] K. F. Warnick, Numerical Analysis for Electromagnetic Integral Equations, Artech House, 2008.

[50] R. Graglia, D. Wilton, A. Peterson, Higher order interpolatory vector bases for computational electromagnetics, IEEE Transactions on Antennas and Propagation 45 (3) (1997) 329–342. doi:10.1109/8.558649.

[51] B. A. Freno, W. A. Johnson, B. F. Zinser, S. Campione, Symmetric triangle quadrature rules for arbitrary functions, Computers & Mathematics with Applications 79 (2020). doi:10.1016/j.camwa.2019.12.021.

[52] B. A. Freno, N. R. Matula, W. A. Johnson, Manufactured solutions for the method-of-moments implementation of the electric-field integral equation, Journal of Computational Physics 443 (2021). doi:10.1016/j.jcp.2021.110538.

[53] B. A. Freno, N. R. Matula, J. I. Owen, W. A. Johnson, Code-verification techniques for the method-of-moments implementation of the electric-field integral equation, Journal of Computational Physics 451 (2022). doi:10.1016/j.jcp.2021.110891.

[54] B. A. Freno, N. R. Matula, Code-verification techniques for the method-of-moments implementation of the magnetic-field integral equation, Journal of Computational Physics 478 (2023). doi:10.1016/j.jcp.2023.111959.

[55] B. A. Freno, N. R. Matula, Code-verification techniques for the method-of-moments implementation of the combined-field integral equation, Journal of Computational Physics 488 (2023). doi:10.1016/j.jcp.2023.112231.

[56] B. A. Freno, N. R. Matula, R. A. Pfeiffer, E. A. Dohme, J. D. Kotulski, Manufactured solutions for an electromagnetic slot model, Journal of Computational Physics 516 (2024). doi:10.1016/j.jcp.2024.113343.

[57] R. F. Harrington, Time-Harmonic Electromagnetic Fields, Wiley–IEEE Press, 2001. doi:10.1109/9780470546710.

[58] W. C. Chew, Waves and Fields in Inhomogenous Media, Wiley–IEEE Press, 1995. doi:10.1109/9780470547052.

[59] C. A. Balanis, Advanced Engineering Electromagnetics, John Wiley & Sons, Inc., 2012.

[60] W. Chew, J. Jin, E. Michielssen, J. Song, Fast and Efficient Algorithms in Computational Electromagnetics, Artech House, 2001.

[61] P. Ylä-Oijala, M. Taskinen, Calculation of CFIE impedance matrix elements with RWG and $\boldsymbol{n}\times$RWG functions, IEEE Transactions on Antennas and Propagation 51 (8) (2003) 1837–1846. doi:10.1109/TAP.2003.814745.

[62] B. A. Freno, N. R. Matula, Code verification for practically singular equations, Journal of Computational Physics 470 (2022). doi:10.1016/j.jcp.2022.111581.

[63] J. N. Lyness, D. Jespersen, Moderate degree symmetric quadrature rules for the triangle, IMA Journal of Applied Mathematics 15 (1) (1975) 19–32. doi:10.1093/imamat/15.1.19.

[64] D. A. Dunavant, High degree efficient symmetrical Gaussian quadrature rules for the triangle, International Journal for Numerical Methods in Engineering 21 (6) (1985) 1129–1148. doi:10.1002/nme.1620210612.

APPENDIX: ADDITIONAL NORMS OF THE DISCRETIZATION ERROR

In Chapter 4, the solution-discretization error is measured using the L^∞ norm of the discretization error $\|\mathbf{e_J}\|_\infty$ (3.10). In this appendix, we measure the L^1 and L^2 norms of the discretization error.

A.1. The Electric-Field Integral Equation

In Figure 4-5, the discretization error for the EFIE cases is measured in the L^∞ norm. In Figure A-1, we measure the discretization error in the L^1 norm, and, in Figure A-2, we measure the discretization error in the L^2 norm. As with the cases in Figure 4-5, the convergence rates are all $\mathcal{O}(h^2)$ as expected.

A.2. The Magnetic-Field Integral Equation

In Figure 4-12, the discretization error for the MFIE cases is measured in the L^∞ norm. In Figure A-3, we measure the discretization error in the L^1 norm, and, in Figure A-4, we measure the discretization error in the L^2 norm. As with the cases in Figure 4-12, the convergence rates are all $\mathcal{O}(h^2)$ as expected.

A.3. The Combined-Field Integral Equation

In Figure 4-14, the discretization error for the CFIE cases is measured in the L^∞ norm. In Figure A-5, we measure the discretization error in the L^1 and L^2 norms. As with the cases in Figure 4-14, the convergence rates are all $\mathcal{O}(h^2)$ as expected.

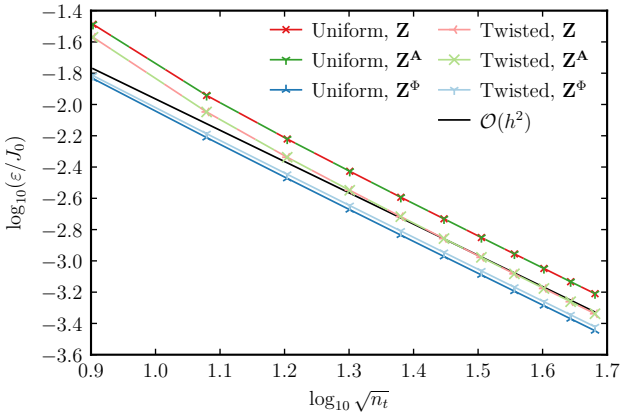

(a) $\theta = 0°$

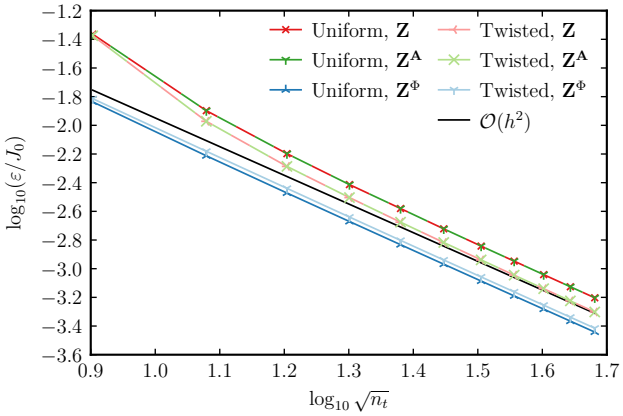

(b) $\theta = 45°$

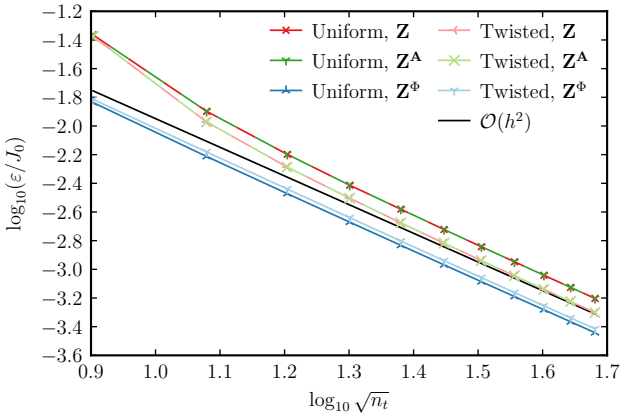

(c) $\theta = 90°$

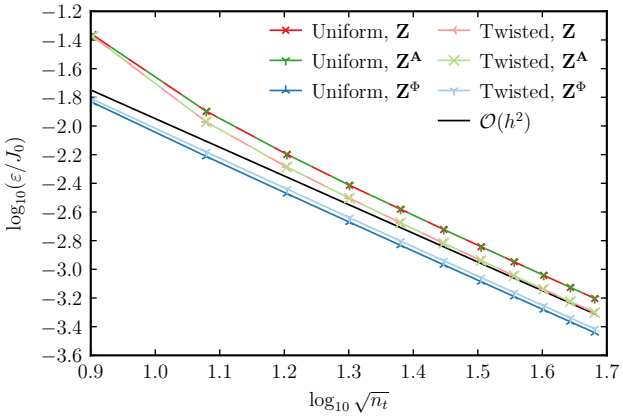

(d) $\theta = 135°$

Figure A-1. EFIE, solution-discretization error: $\varepsilon = \|\mathbf{e}\|_1$ for $q = 2$ in G_{MS} (3.9).

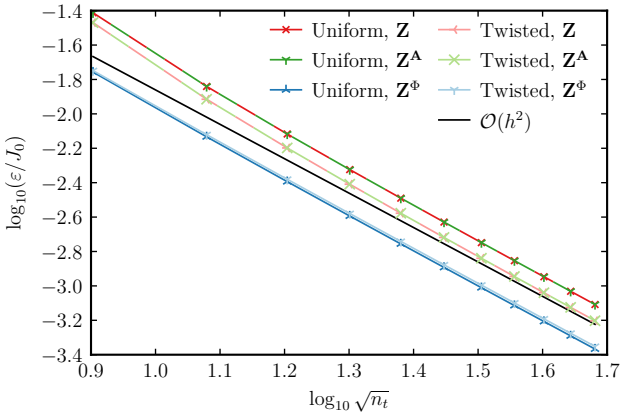

(a) $\theta = 0°$

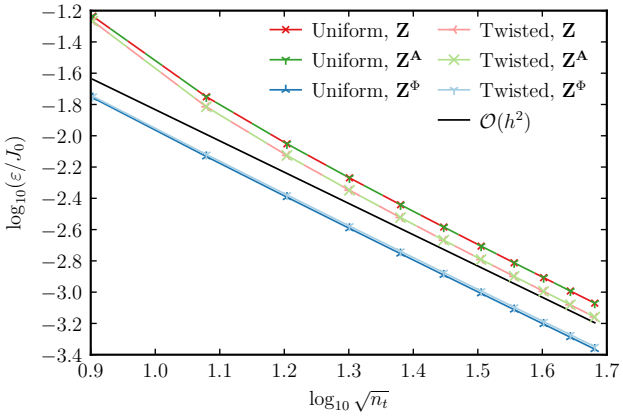

(b) $\theta = 45°$

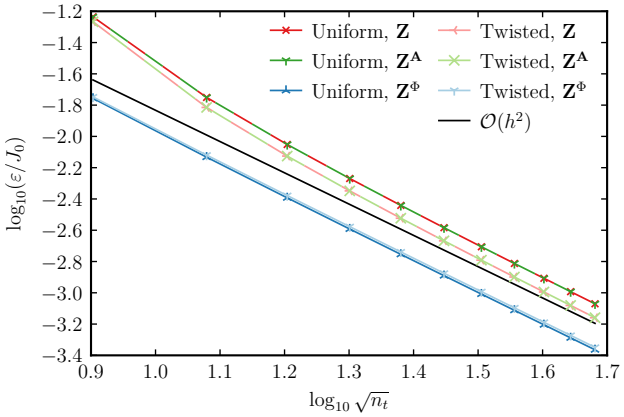

(c) $\theta = 90°$

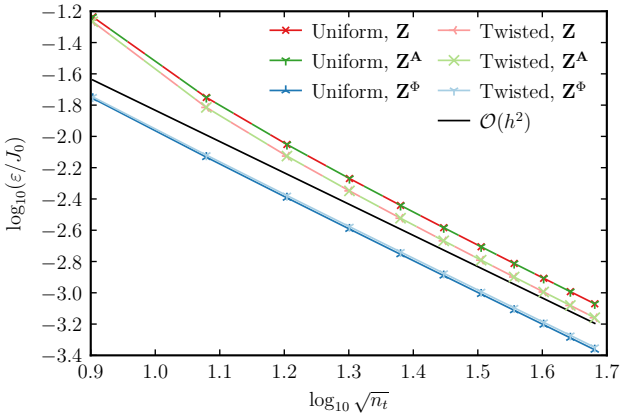

(d) $\theta = 135°$

Figure A-2. EFIE, solution-discretization error: $\varepsilon = \|\mathbf{e}\|_2$ for $q = 2$ in G_{MS} (3.9).

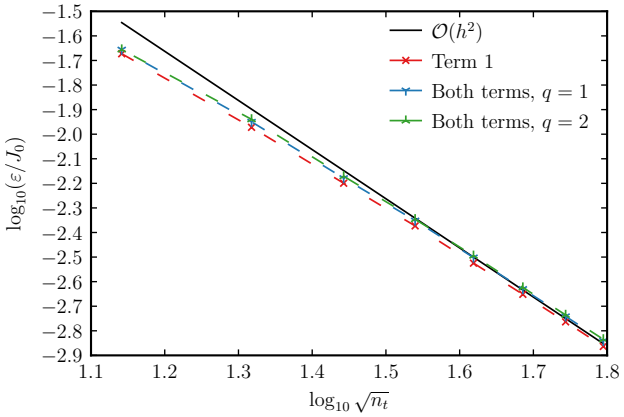

(a) Cube, Term 1 and both terms

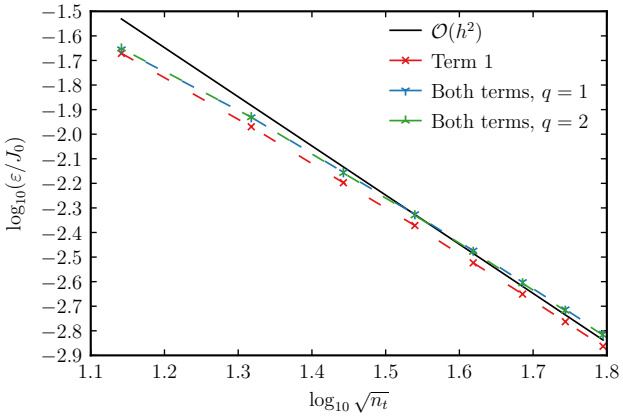

(b) Rhombic prism, Term 1 and both terms

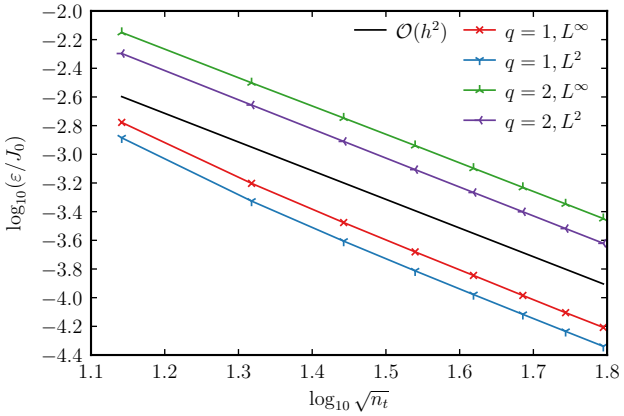

(c) Cube, Term 2

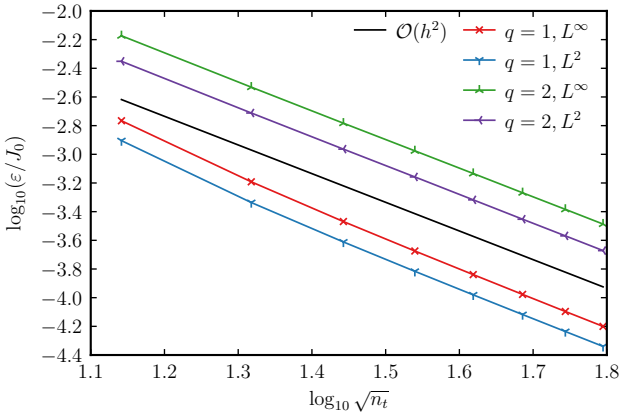

(d) Rhombic prism, Term 2

Figure A-3. MFIE, solution-discretization error: $\varepsilon = \|\mathbf{e}\|_1$ for different term combinations and q values in G_{MS} (3.9). For Term 2, a unique solution is obtained by minimizing $\|\mathbf{e_J}\|_2$ (3.11) and $\|\mathbf{e_J}\|_\infty$ (3.12).

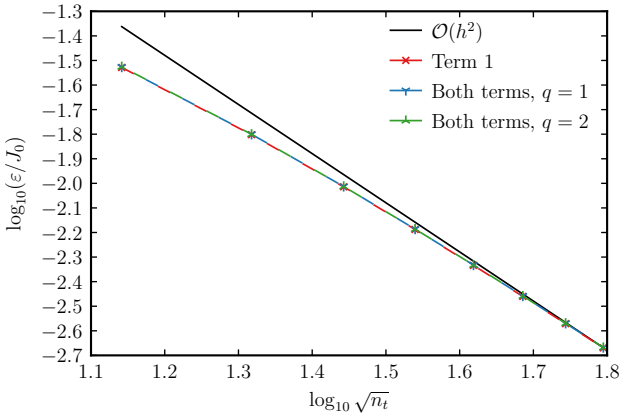

(a) Cube, Term 1 and both terms

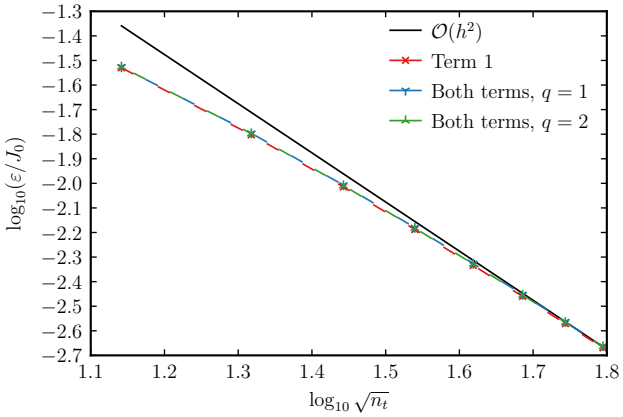

(b) Rhombic prism, Term 1 and both terms

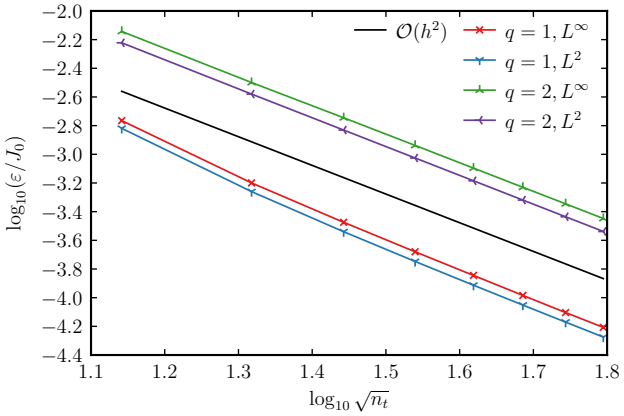

(c) Cube, Term 2

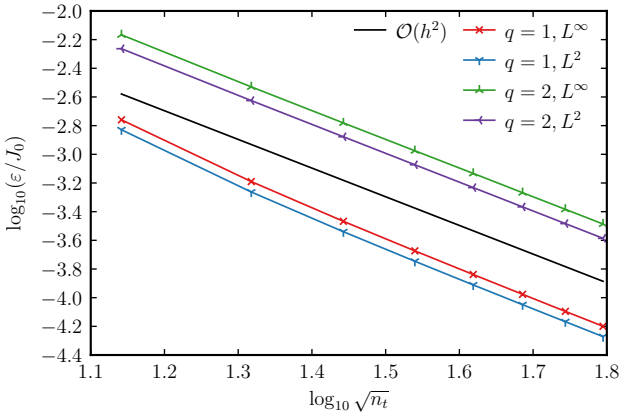

(d) Rhombic prism, Term 2

Figure A-4. MFIE, solution-discretization error: $\varepsilon = \|\mathbf{e}\|_2$ for different term combinations and q values in G_{MS} (3.9). For Term 2, a unique solution is obtained by minimizing $\|\mathbf{e_J}\|_2$ (3.11) and $\|\mathbf{e_J}\|_\infty$ (3.12).

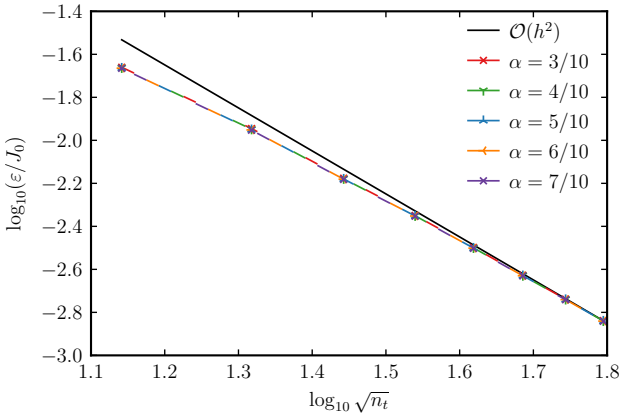

(a) Cube, $\varepsilon = \|\mathbf{e}\|_1$

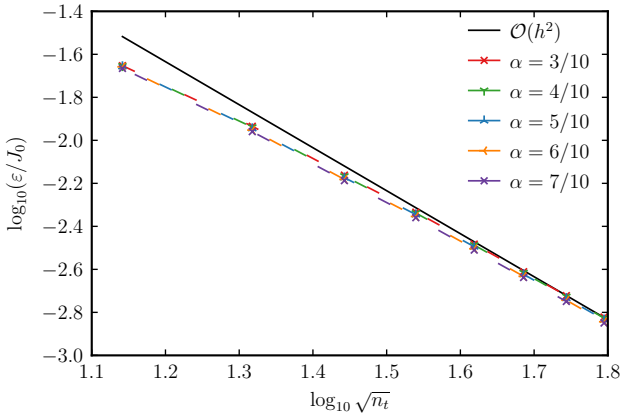

(b) Rhombic prism, $\varepsilon = \|\mathbf{e}\|_1$

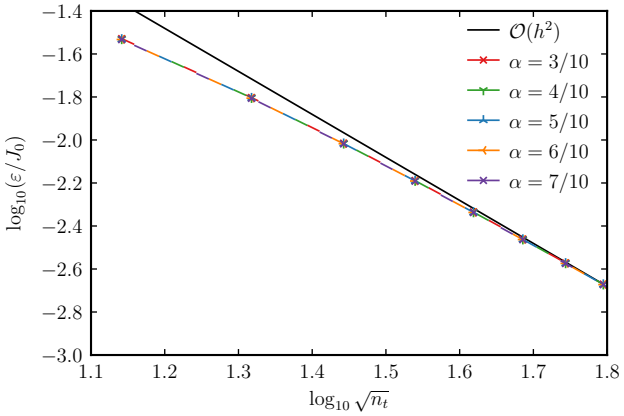

(c) Cube, $\varepsilon = \|\mathbf{e}\|_2$

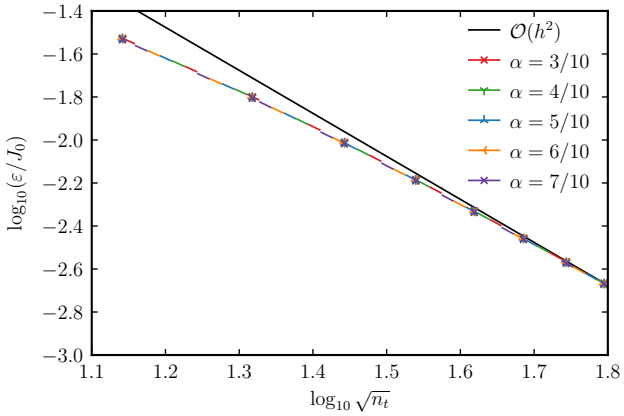

(d) Rhombic prism, $\varepsilon = \|\mathbf{e}\|_2$

Figure A-5. CFIE, solution-discretization error: $\varepsilon = \|\mathbf{e}\|$ for $q = 2$ in G_{MS} (3.9) and different combination parameters α.

DISTRIBUTION

Email – Internal

Name	Org.	Sandia Email Address
Scott Hutchinson	1320	sahutch@sandia.gov
Shawn Pautz	1321	sdpautz@sandia.gov
Alden Roy Pack	1322	arpack@sandia.gov
Duncan McGregor	1323	damcgre@sandia.gov
Keith Cartwright	1324	klcartw@sandia.gov
Evelyn Dohme	1324	eadohme@sandia.gov
Joseph Kotulski	1324	jdkotul@sandia.gov
William Langston	1324	wllangs@sandia.gov
Robert Pfeiffer	1324	rapfeif@sandia.gov
Javier Rivero	1324	frivero@sandia.gov
Heidi Thornquist	1325	hkthorn@sandia.gov
Tom Smith	1446	tmsmith@sandia.gov
Erik Strack	1540	oestrac@sandia.gov
Paul Crozier	1541	pscrozi@sandia.gov
Neil Matula	1541	nmatula@sandia.gov
Brian Carnes	1544	bcarnes@sandia.gov
Brian Freno	1544	bafreno@sandia.gov
Jared Kirsch	1544	jkirsch@sandia.gov
Aaron Krueger	1544	amkrueg@sandia.gov
Kyle Neal	1544	kneal@sandia.gov
Bill Rider	1544	wjrider@sandia.gov
Greg Weirs	1544	vgweirs@sandia.gov
Justin Winokur	1544	jgwinok@sandia.gov
Tricia Gharagozloo	8750	peghara@sandia.gov
Maher Salloum	8751	mnsallo@sandia.gov
Technical Library	1911	sanddocs@sandia.gov

Email – External

Name	Company Email Address	Company Name
Jim Ferguson	jmferguson@lanl.gov	Los Alamos National Laboratory

Sandia National Laboratories

Sandia National Laboratories is a multimission laboratory managed and operated by National Technology & Engineering Solutions of Sandia LLC, a wholly owned subsidiary of Honeywell International Inc., for the U.S. Department of Energy's National Nuclear Security Administration under contract DE-NA0003525.